nature materials

Supplementary information

https://doi.org/10.1038/s41563-024-02025-5

Formation, chemical evolution and solidification of the dense liquid phase of calcium (bi)carbonate

In the format provided by the authors and unedited

Table of Contents

Protein synthesis

DHR49-Neg (fig. S1) was designed by taking an internal helix-turn-helix repeat of scaffold protein DHR49[1] and repeating it in tandem 6 times. Duplicating an internal repeat removes the capping features found in the scaffold protein. One surface of the protein was mutated (while maintaining a repeat sequence) to create the high density of carboxylate acid-containing sidechains, largely from aspartic acid (Asp) residues.

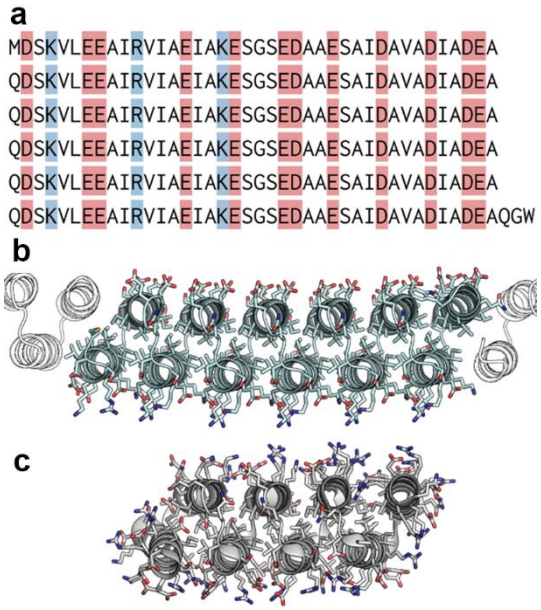

Figure S1. Sequence and structure of aspartate rich, non-capped (NC), designed helical repeat (DHR) protein DHR49-Neg. (a) Full length (243 amino acid) sequence of DHR49-Neg displayed with negative (red) and positive (blue) residues. It has a total of 72 negative sidechains containing carboxylic acid groups and 18 positive sidechains containing amino or guanidino groups and a theorectical isoelectric point (pI) of 3.8. (b) Alpha-fold predicted structure of DHR49-Neg. Each protein is composed of six tandem repeats of a 40 amino-acid helix-turn-helix motif. All of aspartatic acid residues are localized to the upper side of the protein. Helices shown as outlines are from other copies of the protein assembled through head-to-tail interfaces. (c) Structure of the scaffold protein DHR49 (PDB id: 5CWJ)[1] which was modified to create DHR49-Neg.

DNA encoding the amino acid sequence of DHR49-Neg (fig. S1a) was ordered from Genscript cloned in a pet21b plasmid. DHR49-Neg protein was expressed in *E. coli* overnight at 37 °C in Studier's autoinduction media with carbenicillin. 500mL of culture was grown in a 2 L baffled flask shaken at 200 rpm. Cells were pelleted at 4,000g for 20 mins, resuspended in 30 mL lysis buffer (1mg/mL DNAse, 1mM PMSF, 50mM NaCl, 50 mM Tris HCl pH 8), and lysed with a microfluidizer at 18K pounds per inch^2. Lysate was centrifuged at 20,000 *g* for 20 min and the soluble fraction was retained with a serological pipette. The soluble lysate was incubated at 80 °C for 1 hour, spun at 20,000 *g* for 20 min and the soluble fraction was retained. 5 M NaCl was added to adjust the concentration to 1 M to precipitate the DHR49-Neg proteins. After incubating for 1 hour the now cloudy solution was spun at 20,000 *g* for 20 min, and the precipitated protein pellet was retained. The precipitated DHR49-Neg was readily resuspended in 30 mL buffer (50 mM NaCl, 50 mM Tris HCl pH 8). Next, the process from the heat incubation step onward was repeated until the protein pellet was completely white (typically 2-3 times). The final protein pellet was resuspended to 10 mg/mL and sample fractions were further purified with size-exclusion

chromatography (AKTA pure system with a Superdex 200 Increase 10/300 GL column). Eluted DHR49-Neg fractions were pooled and dialyzed extensively against pure H_2O. Four dialysis steps were performed using a 3 mL dialysis cassette with a 3,500 Da molecular weight cut-off (Thermo) in 4 L of milli-Q H_2O.

Supporting TEM images

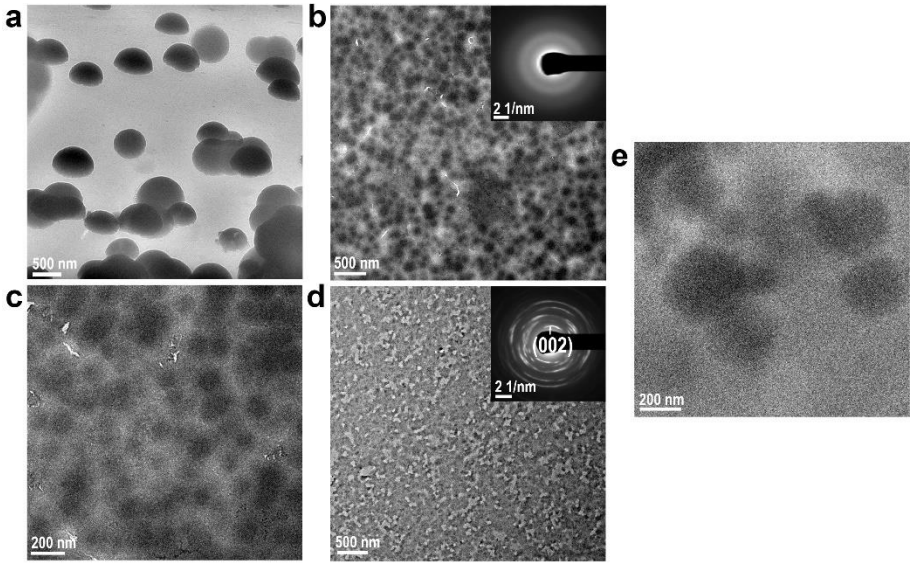

Figure S2. Ex situ TEM images of initially formed particles. (a) Obvious wetting behavior of particles in contact with hydrophilic carbon film processed by plasma cleaner. (b-c) Contineous amorphous film. (d) Contineous vaterite film on carbon film. (e) Cryo-TEM image showing the formation of amorphous particles with the round morphology, low contrast, and diameters in the range of tens to hundreds of nm, which are similar to LP-TEM observations in Figure 1b.

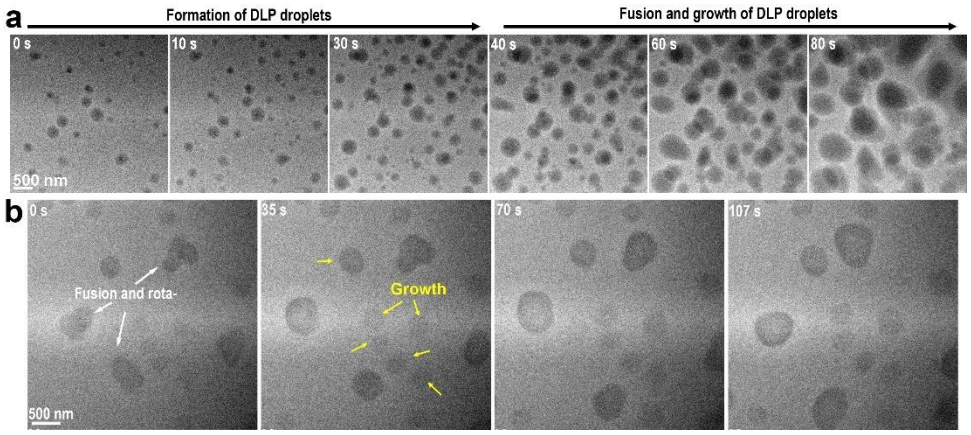

Figure S3. LP-TEM showing the dynamical behavior of DLP droplets in solution in the presence of 0.4 μM DHR49-Neg. (a) The formation and fusion of DLP droplets. (b) The direct growth, fusion and rotation of multiple DLP droplets.

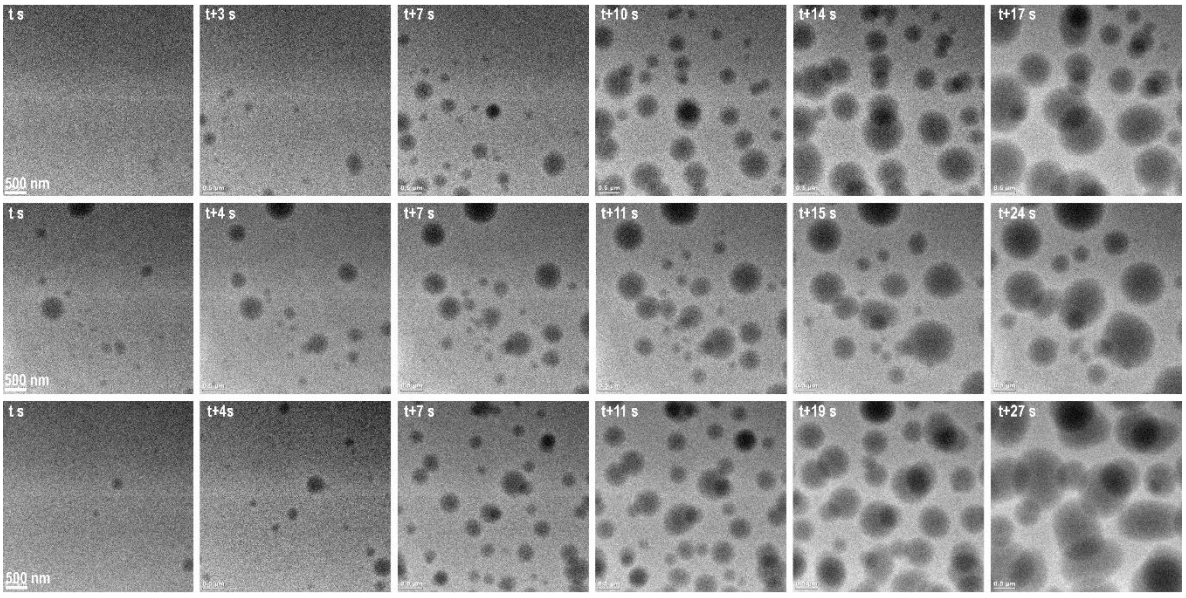

Figure S4. More cases in LP-TEM observations showing the formation and fusion of multiple DLP droplets in the presence of 0.4 μM DHR49-Neg.

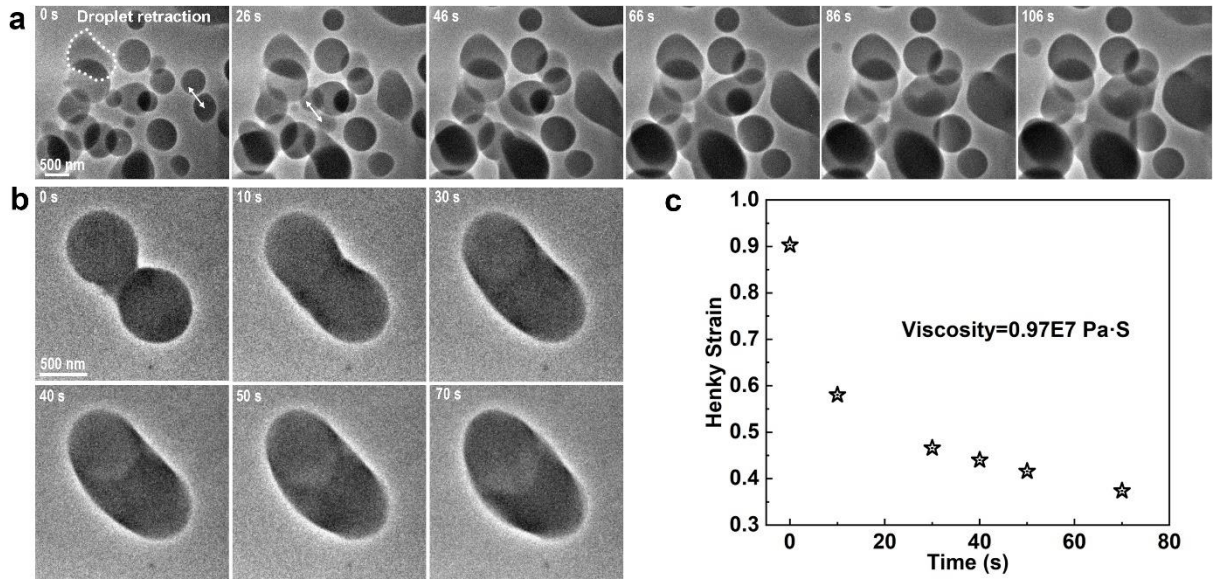

Figure S5. The fusion of DLP droplets in the presence of 0.4 μM DHR49-Neg. (a) Time-dependent TEM images showing the fusion process of DLP droplets. The retraction process of a fused droplet marked by dot lines was used to calculate the DLP viscosity which is indicated by Figure 1E in main text. The fusion of multiple droplets were highlighted by arrows. (b-c) One more case for calculating DLP viscosity.

Comparison of droplet sizes in various experimental environments

DLP droplet sizes in LP-TEM vs bulk solutions or NMR tubes: DLP droplet sizes in TEM can reach the micrometer range but are probably influenced by the depletion of the solute ions in the small liquid cell volume, the state of quiescence of the liquid, the presence of surfaces, and the time it takes for solidification to begin. We did not attempt to compare the size distribution of droplets seen in TEM with observations on bulk solution by, for example, dynamic light scattering, or in NMR experiments by deconvolving the signals from surface atoms and bulk atoms[2], because, unlike growth in a two-phase "solid-plus-liquid" region of a phase diagram where (assuming adequate mixing) growth is controlled by the interface kinetics, in the LLPS region, it is controlled by mass transport which will be affected by the different volumes and geometries of liquid cells for microscopy and those for bulk measurements. Moreover, such measurements fail to provide information on either the nature of the particles formed (i.e., liquid vs. solid) or particle chemistry and its evolution and droplet sizes should vary in the different reaction stages and environments.

The estimation of viscosity of DLP droplets

Due to the comparable density of DLP droplets and water, we used a Hencky strain model to estimate the viscosity of the droplets. According to the previous report[3], we define Hencky strain as $H = \ln L_1 / 2r_0$, where L_1 is the length of the long axis of a deformed droplet, and r_0 is the radius of the undeformed spherical particle. The relaxation is expected to obey:

$$H = H_0 e^{(t/\tau_2)}$$

Where the relaxation timescale is:

$$\tau_2 = \frac{r_0 \eta_m}{\gamma} \frac{\left(19\frac{\eta_d}{\eta_m} + 16\right)\left(2\frac{\eta_d}{\eta_m} + 3\right)}{40\left(\frac{\eta_d}{\eta_m} + 1\right)}$$

γ = interfacial tension of droplet

η_m = viscosity of H_2O (~0.001 Pa·s in bulk at room temperature)

η_d = viscosity of DLP droplet

In simplifying case where $\eta_m \ll \eta_d$

$$\tau_2 = \frac{r_0 \eta_d}{\gamma} \frac{19}{20}$$

Solving for viscosity:

$$\eta_d = \frac{20\gamma\tau_2}{19r_0}$$

For the present case examined (Fig. S5a, table S1 and Fig. 1e), τ_2 is fitted to about 102 s from exponential fitting in Fig. 1e and thus:

$$\eta_d = \frac{20 \cdot (0.012\ \mathrm{J/m^2}) \cdot (102\ \mathrm{s})}{19 \cdot (820 \cdot 10^{-9}\ \mathrm{m})} = 1.56 \cdot 10^6\ \mathrm{Pa \cdot s}$$

This is dramatically higher than the viscosity of water (0.0001 Pa·s), and so we can assume the approximation of $\eta_m \ll \eta_d$ holds. Another case gives a viscosity of $1.2 \cdot 10^6$ Pa·s (fig. S5b-c). In this calculation, we assumed the interfacial tension of DLP droplets to be 12 mJ/m^2, which is equal to that of hydrated ACC and gives a droplet stiffness of 20 mJ/m^2.[4-5]

Notably, some — or perhaps all — droplets interact with the upper or lower membranes of the liquid cell, resulting in a slower relaxation dynamics and thus slower evolution of the Hencky strain. However, the calculation of Hencky strain and the fit of the data to obtain the viscosity assume that the droplets are free in solution. Therefore, the calculated viscosity is an upper limit and the actual viscosity should be lower than ~10^6 Pa·s.

Table S1. The length change during fused droplet retraction process and calculated Hencky strain

Time (s)	L_1 long Axis (nm)	L_2 Short Axis (nm)	H (Hencky Strain)
0	961	642	0.2689241
26	959	693	0.2165741
46	982	757	0.1734854
66	968	795	0.13126
86	990	812	0.1321364
106	960	837	0.0914061

^{13}C NMR chemical shift: coordinating HCO_3^- vs. free HCO_3^-

Based on the ^{13}C chemical shift $\delta(^{13}C)$ of HCO_3^- at pH 5.0 (161.08 ppm) and $\delta(^{13}C)$ of CO_3^{2-} at pH 14.0 (169.08 ppm) and recognizing that the apparent $\delta(^{13}C)$ is a weighted average of $\delta(HCO_3^-)$ and $\delta(CO_3^{2-})$, we calculated $\delta(^{13}C)$ as a function of fraction of CO_3^{2-} (fig. S6a). Coordination to Ca^{2+} may shift $\delta(CO_3^{2-})$ between 167.98 ppm and 171.10 ppm, as observed in ACC or monohydrocalcite[7], but because no other resonance was detected between 160 – 170 ppm (fig. S7), the signal between 161.10 and 161.40 ppm reveals that HCO_3^- dominates (> 96%) and that no liquid-phase CO_3^{2-} was detected during the reaction.

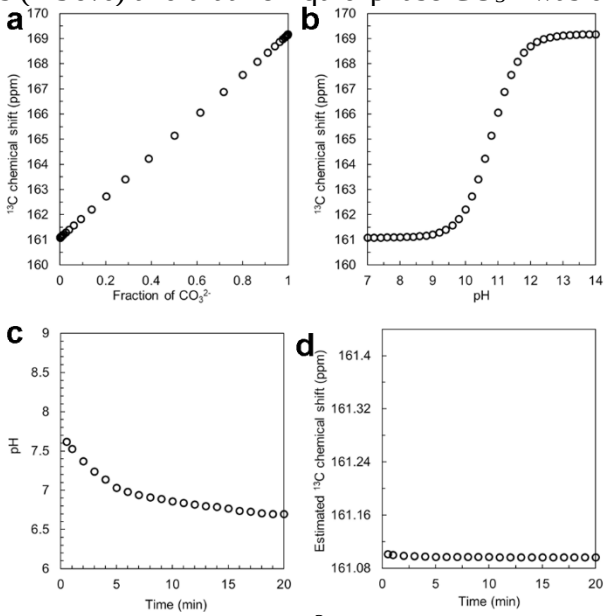

Figure S6. $\delta(^{13}C)$ as a function of (a) fraction of CO_3^{2-} and (b) solution pH, estimated based on $\delta(^{13}C)$ of pure HCO_3^- at pH 7.0 (161.10 ppm) and pure CO_3^{2-} at pH 14.0 (169.18 ppm), as well as the equilibrium constant of $HCO_3^- \rightarrow CO_3^{2-} + H^+$ (1.60×10^{-11}). (c) Measured pH changes and (d) calculated $\delta(^{13}C)$ based on the measured pH values over time after mixing 100 mM $NaHCO_3$ and 100 mM $CaCl_2$.

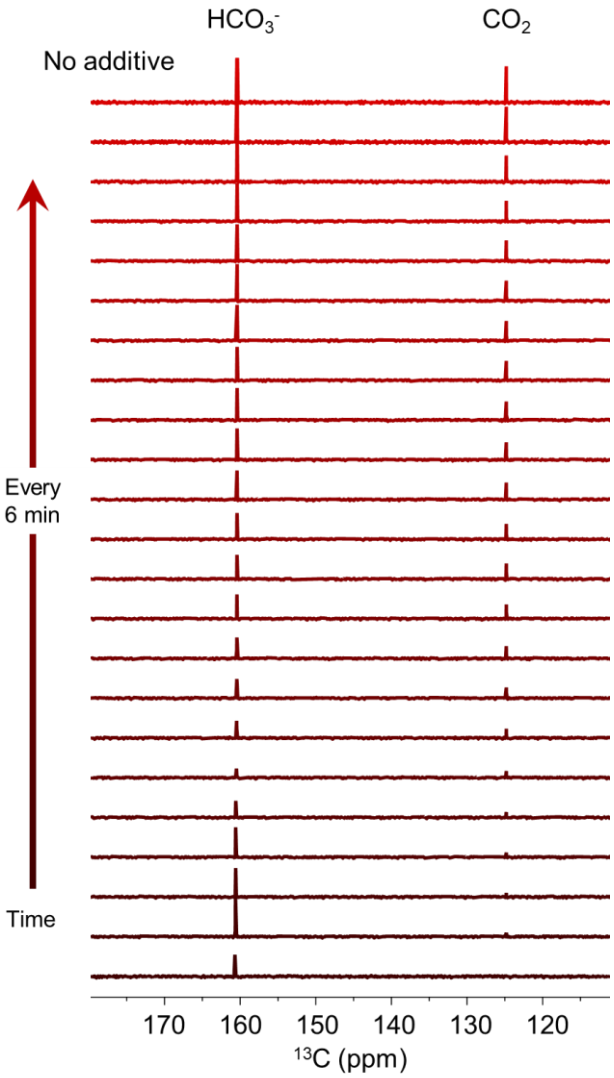

Figure S7. Time dependent ^{13}C NMR spectra after mixing 100 mM $NaHCO_3$ (pH 8.7) and 100 mM $CaCl_2$ (pH 6.9), same as Fig. 2a but the broader range showing that no liquid-phase CO_3^{2-} (including DLP) is detected during the reaction.

After considering the isotope effect of D_2O vs H_2O on the dissociation constant of HCO_3^-[8,9], $\delta(^{13}C)$ as a function of pH is calculated using 1.60×10^{-11} for K_2 (HCO_3^-) (fig. S6b). Along with the measured pH change with time 7.6 to 6.9 (fig. S6c), we can see that the estimated $\delta(^{13}C)$ based on pH only changed slightly from 161.11 to 161.10 ppm with time when the exchange between free HCO_3^- and CO_3^{2-} is the only factor influencing $\delta(^{13}C)$ (fig. S6d). When comparing the first ^{13}C spectrum after mixing $NaHCO_3$ with $CaCl_2$ and with NaCl (fig. S8), the shift of 0.29 ppm to a higher frequency in the mixed solution with $CaCl_2$ is clear evidence that this 161.40 ppm signal can be attributed to HCO_3^- in a different coordination environment (coordinating to Ca^{2+}) than that of free HCO_3^-. Previous quantum mechanical calculations of chemical shifts also reported a difference of less than 0.30 ppm in $\delta(^{13}C)$ when substituting Na^+ for Ca^{2+} at a remote site from HCO_3^-[10].

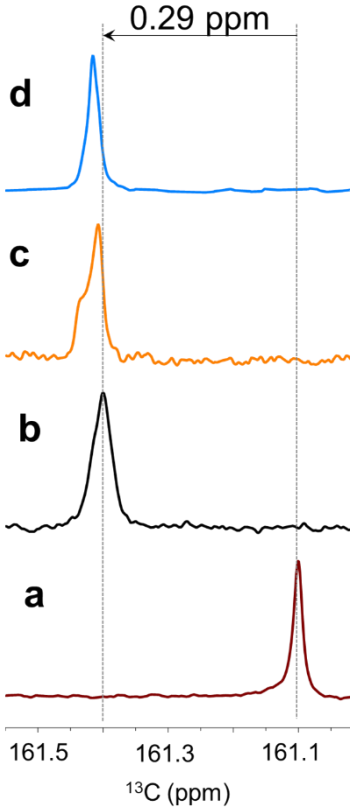

Figure S8. The first ^{13}C NMR spectra after mixing 100 mM $NaHCO_3$ (pH 8.7) and 100 mM $CaCl_2$ (pH 6.9) with and without additives along with 150 mM NaCl (pH 6.9) for comparison. (a) 100 mM $NaHCO_3$ (pH 8.7) and 150 mM NaCl (pH 6.9). (b) 100 mM $NaHCO_3$ (pH 8.7) and 100 mM $CaCl_2$ (pH 6.9). (c) 100 mM $NaHCO_3$ with 0.8 μM DHR49-Neg (pH 8.7) and 100 mM $CaCl_2$ (pH 6.9). (d) 100 mM $NaHCO_3$ with 5 μg/ml 1.8 kDa PAA (pH 8.7) and 100 mM $CaCl_2$ (pH 6.9). The first scans are acquired at ~1 min after mixing.

In addition, because coordinated HCO_3^- may exchange with free HCO_3^-, which is located at 161.11 – 161.10 ppm over the pH range used here, the observed signal could be a weighted average of both. The shift of the center of gravity of the signal from 161.40 to 161.10 ppm with time (Fig. 2b) may reflect the change in the fraction of the coordinating HCO_3^-, but it could also be resulted from the distribution of HCO_3^- located within different dense liquid droplets. Compared to the well-defined sharp Lorentzian-shaped CO_2 resonance at 125.50 ppm (fig. S9), the HCO_3^- ^{13}C resonance broadens in the first 20 – 30 min

and then sharpens again, consistent with polymorphic HCO_3^- environments within a heterogeneous distribution of droplet sizes, causing multiple spectral components.

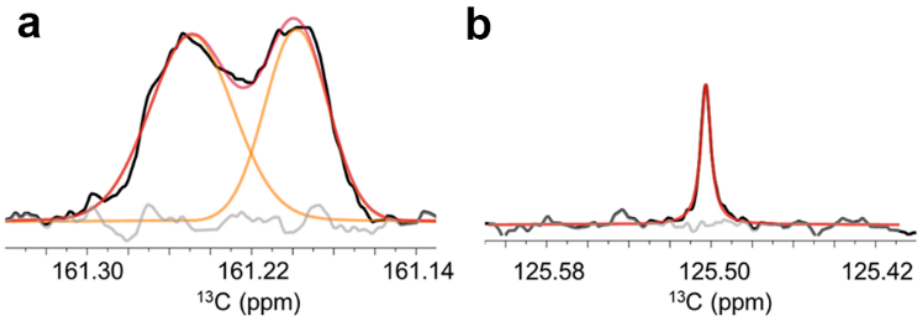

Figure S9. Line fitting of ^{13}C resonances of HCO_3^- within DLP (a) and dissolved CO_2 (b) at 30 minutes after mixing 100 mM $NaHCO_3$ and 100 mM $CaCl_2$.

^{43}Ca NMR chemical shift: coordinating Ca^{2+} vs. free Ca^{2+}

Due to the very low natural abundance of ^{43}Ca (0.135%), a measurement time of about 15 hours is required to acquire a ^{43}Ca NMR spectrum with a reasonable signal to noise ratio for the natural-abundant solutions of 50 mM Ca^{2+}. Comparison between the ^{43}Ca NMR spectra of 50 mM $CaCl_2$, 100 mM $CaCl_2$ with 100 mM $NaHCO_3$ in the absence and presence of PAA (fig. S10) shows that a significant amount of Ca^{2+} precipitate as $CaCO_3$ in the solution with no PAA, the remaining Ca^{2+} in the solution is consistent with the solubility of $Ca(HCO_3)_2$ (10 mM) at 25 °C[11,12]. In contrast, 25 μg/mL 1.8 kDa PAA (350 μM COO^-) allows the majority of 50 mM Ca^{2+} to stay in the solution during the measurement. A shift of 0.44 ppm in the ^{43}Ca spectrum with PAA to a higher frequency suggests that Ca^{2+} experience different coordination environment from fully solvated Ca^{2+} in water. A similar observation was reported recently, where the addition of L-Asp caused a shift of 0.1 ppm to a higher frequency and the shift was attributed to the complexation of Ca^{2+} with COO^- from L-Asp[13]. Combined with $\delta(^{13}C)$ of HCO_3^- which maintains a shift of 0.1 – 0.3 ppm to a higher frequency (from free HCO_3^-) for 10 hours after mixing, we may conclude that the Ca^{2+} coordinate to carboxyl groups from PAA and HCO_3^- in solution for about 10 hours. Considering the small molar ratio of COO^- from PAA to Ca^{2+} (1: 143), the stabilization capability of PAA is extremely powerful.

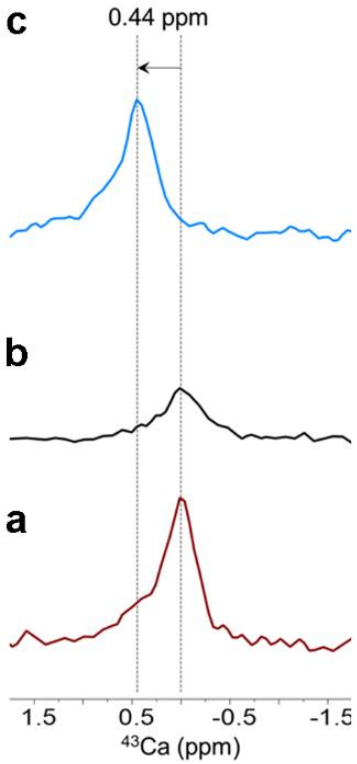

Figure S10. ^{43}Ca NMR spectra of $CaCl_2$ (50 mM) and the mixed solutions of $NaHCO_3$ and $CaCl_2$ in the absence and presence of PAA. Because the experimental time was 15 hr for each spectrum, we could not detect the change in ^{43}Ca with time. During the 15 hr of measurements, the smaller ^{43}Ca signal of the solution of $CaCl_2$ and $NaHCO_3$ with no additives is caused by the precipitation of $CaCO_3$, the remaining 20 – 30% signal is consistent with the solubility of $Ca(HCO_3)_2$ (~10 mM). (a) 50 mM $CaCl_2$ (pH 6.9). (b) 100 mM $NaHCO_3$ (pH 8.7) and 100 mM $CaCl_2$ (pH 6.9). (c) 100 mM $NaHCO_3$ with 50 μg/ml 1.8 kDa PAA (pH 8.7) and 100 mM $CaCl_2$ (pH 6.9).

In-situ solid-state MAS NMR observation of ACC and calcite

Equal volumes of 100 mM $CaCl_2$ and 100 mM ^{13}C-enriched $NaHCO_3$ in 90% D_2O (10% H_2O) solutions were mixed in a 5 mm *WHiMS* NMR rotor (which can prevent liquid from leakage during spinning)[15] and time-resolved ^{13}C single-pulse NMR were then carried out immediately at a spinning speed of 3550 Hz with an interval of 5 – 6 minutes between each ^{13}C scan and 4 – 8 scans for each spectrum.

In the case of lower pH, we observe the same decrease in HCO_3^- (liquid) and increase in CO_2 (dissolved gas) with time as in the liquid-state NMR, but we also detect an increase in a broader signal located at 168.7 ppm (fig. S11a), which can be assigned to well-crystalized calcite. On the other hand, at a higher pH, we observe an even broader signal at 167 – 170 ppm, and all three signals do not experience significant change with time (fig. S11d). The signal averaging for the next 18 hours increases the signal to noise ratio of the ^{13}C spectra for quantitative analysis (fig. S11b and S11e). As expected, the molar ratio of $CaCO_3$ and CO_2 is close to 1:1 at the lower pH (table S2) because $CaCO_3$ are mainly produced from the decomposition reaction within $Ca(HCO_3)_2$ DLP. In contrast, $CaCO_3$ dominates with a small amount of CO_2 (less than 10%) at the higher pH, and the two relatively broader signals at 168.4 ppm and 169.0 ppm are consistent with the broad signals of pc-ACC (proto-calcite ACC, at 168.7 ppm) and pv-ACC (proto-vaterite ACC at 169.5 ppm) observed by D. Gebauer *et. al.*[20] In their work, the ACC were quenched by ethanol, then washed and dried before MAS measurement. In our experiment, the ACC were left in the reaction solution, therefore the additional water surrounding ACC could cause the smaller linewidth and the ~ 0.5 ppm difference in the ^{13}C chemical shift. However, since the ACC in our experiments were precipitated instantaneously from a very high level of supersaturation (50 mM Ca^{2+} and 25 mM CO_3^{2-}), we do not expect to observe distinct short-range structures in these ACC. Nevertheless, the two distinguishable ^{13}C signals show that $Ca{\cdot}CO_3$ are present in at least two different types of local environments in the ACC precipitated from high supersaturation and left in the solution. On the other hand, the well-defined calcite are formed slowly from the $Ca(HCO_3)_2$ DLP.

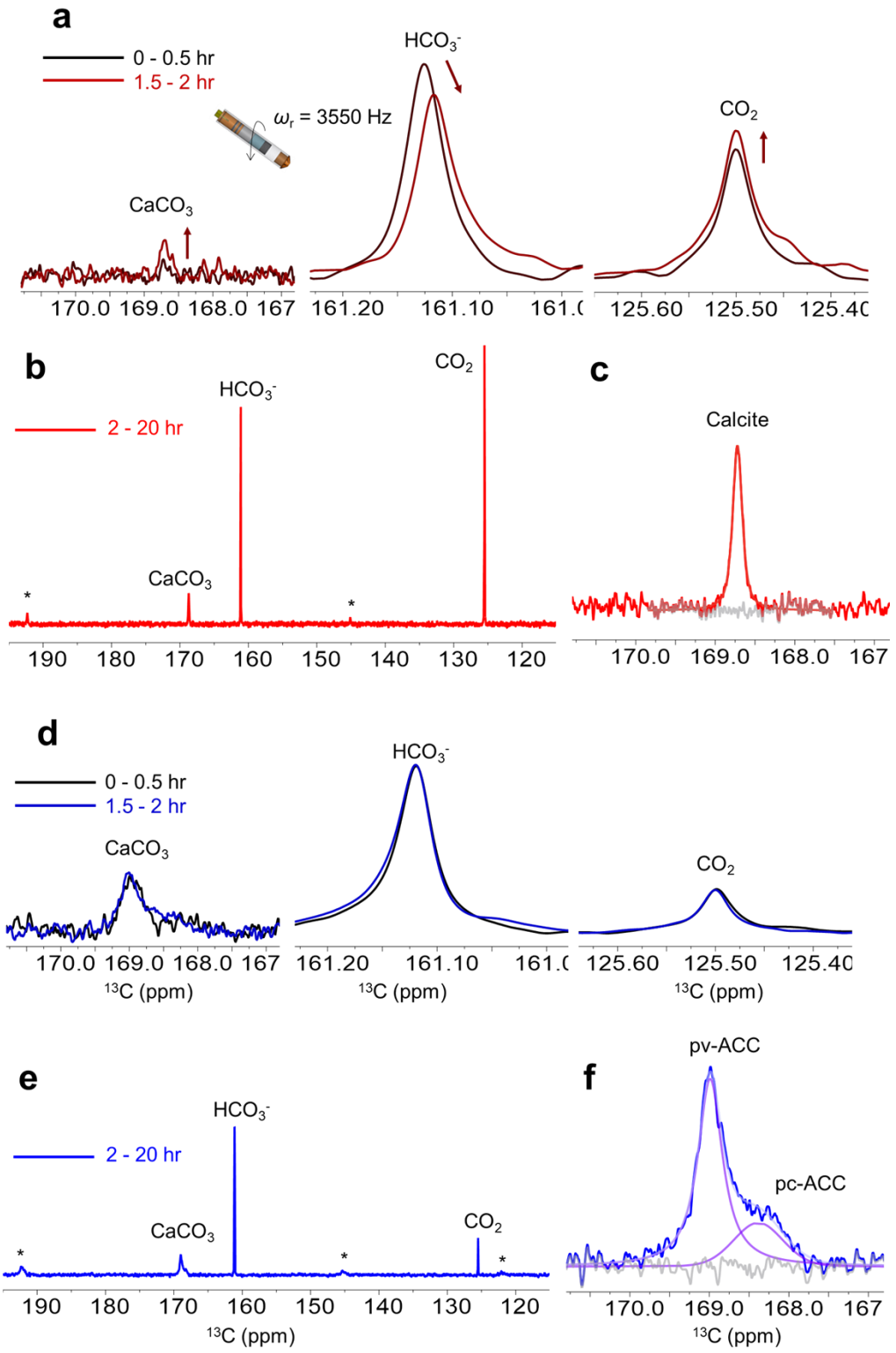

Figure S11. In-situ solid-state MAS ^{13}C spectra of the mixture 100 mM $NaHCO_3$ at pH 8.7 and 100 mM $CaCl_2$ at pH 6.9 collected after mixing for varying times (a-b) and of the mixture 100 mM $NaHCO_3$ at pH 10.8 and 100 mM $CaCl_2$ at pH 6.9 (d-e). Line fitting of the $CaCO_3$ resonances reveals a well-crystalized species with relatively sharp peak at the lower pH (c) and two ACC species with relatively broad peaks at

the higher pH (f). The measurements were performed at a spinning speed of 3550 Hz, with spinning side bands of $CaCO_3$ resonances marked with asterisks in (b) and (e). Experimental time was 0.5 hr for each spectrum in (a) and (d), and 18 hr in (b) and (e).

Table S2. The fraction of $CaCO_3$, HCO_3^- and CO_2, together with $\delta(^{13}C)$, linewidth, estimated species of the $CaCO_3$ resonances obtained from ^{13}C spectra.

Mixture of 100 mM $CaCl_2$	$CaCO_3$ (%)	HCO_3^- (%)	CO_2 (%)	$\delta(^{13}C)$ of $CaCO_3$ (ppm)	Linewidth of $CaCO_3$ (Hz)	Species
$NaHCO_3$ (100 mM, pH 8.7)	34	30	36	168.7	21	calcite
$NaHCO_3$ (100 mM, pH 10.8)	70	24	6	169.0, 168.4	56, 110	pv-ACC, pc-ACC[2,20]

In-situ solution NMR monitoring of DLP formation and transformation at 5 °C

While ^{13}C and ^{43}Ca NMR can distinguish between ion pairs ($Ca{\cdot}HCO_3$) and free ions (HCO_3^- and Ca^{2+}) based on the chemical shifts, it is unlikely to distinguish between ion pairs in bulk solution – $Ca{\cdot}HCO_3$ (aq), and ion pairs within DLP – $Ca{\cdot}HCO_3$ (DLP) due to the rapid exchange between them. To directly detect the transition from $Ca{\cdot}HCO_3$ (aq) to $Ca{\cdot}HCO_3$ (DLP), we lower the temperature to 5 °C with the intention of slowing down the nucleation process as well as the exchange between the two species so that we can detect both. The ^{13}C spectra collected for 370 min after mixing the fresh-prepared 100 mM $NaHCO_3$ and $CaCl_2$ at 5 °C are shown in fig. S12. First, we can see that lowering the temperature from 25 °C to 5 °C indeed increases the "incubation" time from 25-30 min to 140-150 min due to the slower motions of water and ions. During this delay period, we can see that the relatively sharp signals between 160.60 – 160.55 ppm decrease with time, meanwhile the much broader signals between 160.55 – 160.30 ppm increase with time. A zoom-in on the broad signals in fig. S13a show that a broad shoulder appears at 26 min and grows at the cost of the sharp signal at the lower frequency, which completely disappears at 136 min. The line fitting of the spectra (fig. S13b-d) show that the fraction of the broad signal increases from 64% at 70 min to 72% at 92 min and 82% at 114 min. This trend suggests that the sharp signals are related to $Ca{\cdot}HCO_3$ (aq) and the broad signals arise from $Ca{\cdot}HCO_3$ (DLP), therefore what we are seeing is the growth of DLP with a drain of $Ca{\cdot}HCO_3$ (aq). The multiple components of the broad signals can be explained by various $Ca{\cdot}HCO_3$ ions located in slightly different local environments within the DLP droplets of different sizes, as we have observed in LP-TEM, where the droplets have different sizes and can diffuse, grow, and merge inside (Fig. 1 and Fig. S3-4).

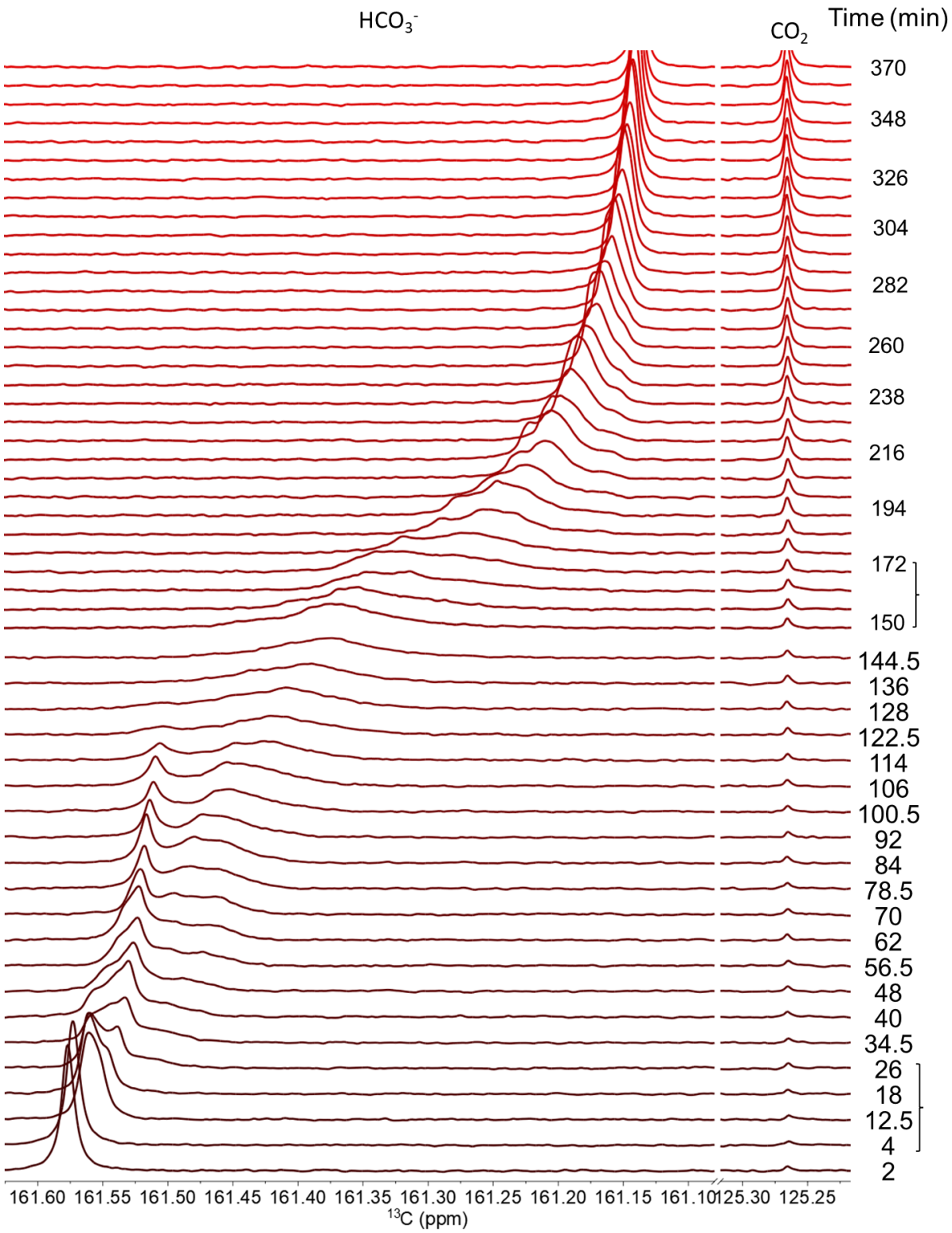

Figure S12. ^{13}C spectra collected at 5 ^{o}C after mixing fresh-prepared 100 mM $NaHCO_3$ (pH 8.7) and 100 mM $CaCl_2$ (pH 6.9) in 90% H_2O and 10% D_2O. Note here the spectra after 150 min are more densely packed than the spectra before 150 min to accommodate all spectra within the page.

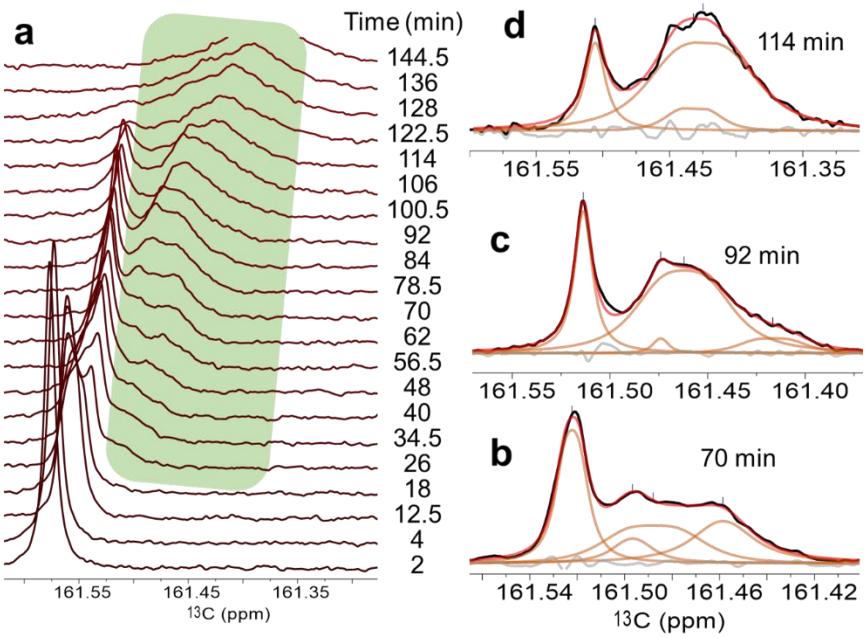

Figure S13. (a) The "zoom-in" of part of Figure S12 to focus on the growth of the broad signal with time. (b-d) Line fitting of ^{13}C resonances of HCO_3^- at 70 min, 92 min and 114 min at 5 °C after mixing the solutions showing the growth of the broad signal as the sharp signal decreases in intensity.

We also performed ^{13}C T_2 measurements and diffusion experiments over the course of the reaction to better evaluate these signals. At 5 °C, ^{13}C T_1 of HCO_3^- is measured to be 15 s, therefore an ideal measurement of ^{13}C T_2 using pulse sequence "cpmg" or diffusion measurements using pulse sequence "ledbpgp2s" with 16 scans (for complete phase cycling), 8 increments, and relaxation delay of 5 T_1 (75 s) will take 160 min, which is not feasible for the in-situ reaction monitored here. We have tested different parameters using a solution of 50 mM $NaHCO_3$ and 150 mM NaCl (which has the same ionic strength as 50 mM $CaCl_2$), and we are able to obtain a ^{13}C T_2 measurement within 6.5 min and a ^{13}C diffusion measurement within 6 min that produce a result within ±5% of an ideal measurement (fig. S14a-b). For ^{13}C T_2, we used an interpulse delay of 5 ms, a relaxation delay of 20 s, 2 scans, and 8 increments (the first three increments are used for the equilibrium of magnetization, similar to the role of dummy scans, and are deleted during the data analysis). For ^{13}C diffusion measurements, we used a diffusion time of 1 s to reach an attenuation of 85% (~15% signal left for the last increment) and compared two sets of parameters: one set with 8 dummy scans, 4 scans, 5 s relaxation delay, and 8 increments, and another set with 4 dummy scans, 2 scans, 20 s relaxation delay and 4 increments. Both produced comparable results. The reaction time during the measurements that were used for data analysis was only 200 s and 160 s for ^{13}C T_2 and diffusion, respectively. Although the reaction continues during the measurements, which would definitely restrict the accuracy of the measurements, the reaction is slow enough (with a pre-nucleation process of ~150 min) that the 2D measurements can detect the changes over the entire reaction time. ^{1}H T_2 was also measured to study the involvement of water during nucleation, with an experimental time of 4.5 min. Each 2D measurement was sandwiched by two ^{13}C 1D spectra to monitor the change of ^{13}C species over the 2D measurements. Each ^{13}C 1D spectrum was collected as a single scan, the 2 min pre-scan (relaxation delay)

after ^{13}C T_2 and diffusion measurements were used to re-equilibrate the ^{13}C magnetization after 2D measurements, and a 1 min pre-scan delay after ^{1}H T_2 as used to remove the Nuclear Overhauser effect (NOE) from ^{1}H to ^{13}C. fig. S14c shows a series of experiments during the reaction monitoring, where each loop took 22 min, so we had around 7 loops during the pre-nucleation process at 5 °C.

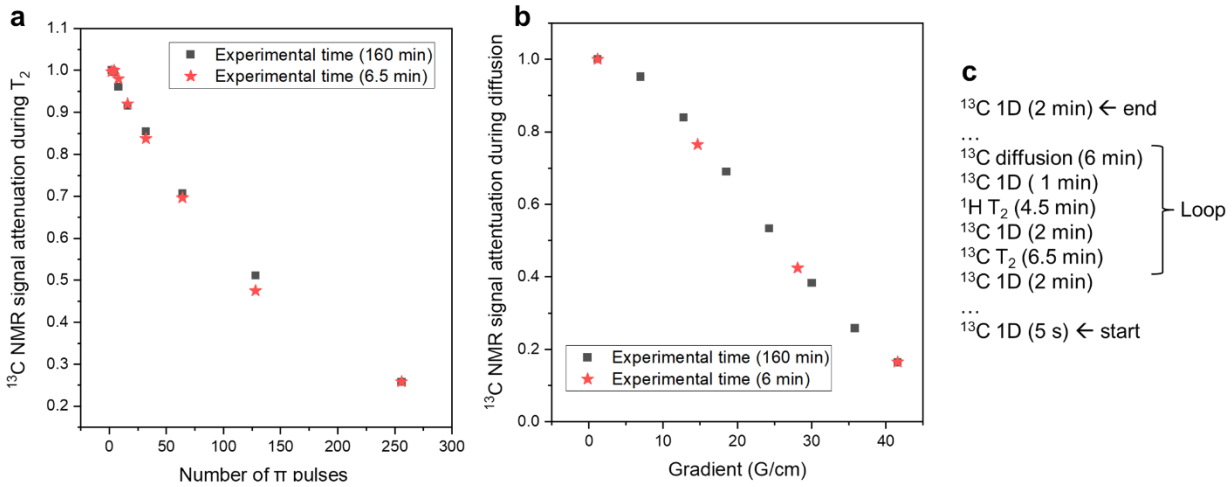

Figure S14. (a) ^{13}C NMR signal attenuation during T_2 measurements for an ideal experiment (160 min) and a short experiment (6.5 min) in 50 mM $NaHCO_3$ and 150 mM NaCl. (b) ^{13}C NMR signal attenuation during diffusion measurements for an ideal experiment (160 min) and a short experiment (6 min). (c) The order of in-situ reaction monitoring experiments for ^{13}C single-pulse 1D, ^{13}C T_2, ^{13}C diffusion and ^{1}H T_2 experiments.

During the period of 62 – 122 min, when the two signals can be clearly detected, we can measure the ^{13}C T_2 and diffusion from the two signals separately. As shown in fig. S15, ^{13}C spectra do not experience significant shifts during the measurements, indicating that no remarkable speciation change occurs as we keep the experimental time at a few minutes. The broad signals have an averaged shorter ^{13}C T_2 value compared to the sharp signal, which can be explained by the broad signals arising from the DLP experiencing restricted motions and larger chemical shift anisotropy (CSA) due to the interactions within the more viscous droplets. On the other hand, the two signals exhibit the same diffusion coefficient, 5.3×10^{-10} m^2/s at 94 – 97 min. This is caused by the exchange of HCO_3^- between the different environments. During NMR diffusion measurement, we use a diffusion time of 1 s, leading to a diffusion length $L = \sqrt{6D_{\text{eff}}t}$ ~32 μm, meaning that HCO_3^- diffuses across ~32 μm during the measurement. Since the size of DLP is on the scale of 100 nm, HCO_3^- goes through multiple stages of $Ca{\cdot}HCO_3$ (DLP) and $Ca{\cdot}HCO_3$ (aq.) during the diffusion measurement. Therefore, the observed diffusion coefficient is a weighted average of all observable HCO_3^-. Even with the shortest diffusion time feasible for NMR PFG diffusion (5 ms), the diffusion length is 2.2 μm with $D \sim 5 \times 10^{-10}$ m^2/s, therefore PFG NMR cannot distinguish between the diffusion within and outside of DLP. Besides, because the aqueous ions have a longer ^{13}C T_1 and T_2, their signals are weighted more at the diffusion measurements where T_1 relaxation occurs at the 1 s diffusion time and T_2 relaxation occurs at the 25 ms gradient duration and stabilization time. Therefore, the obtained $D \sim 5 \times 10^{-10}$ m^2/s is the upper limit for HCO_3^- diffusing within the droplets.

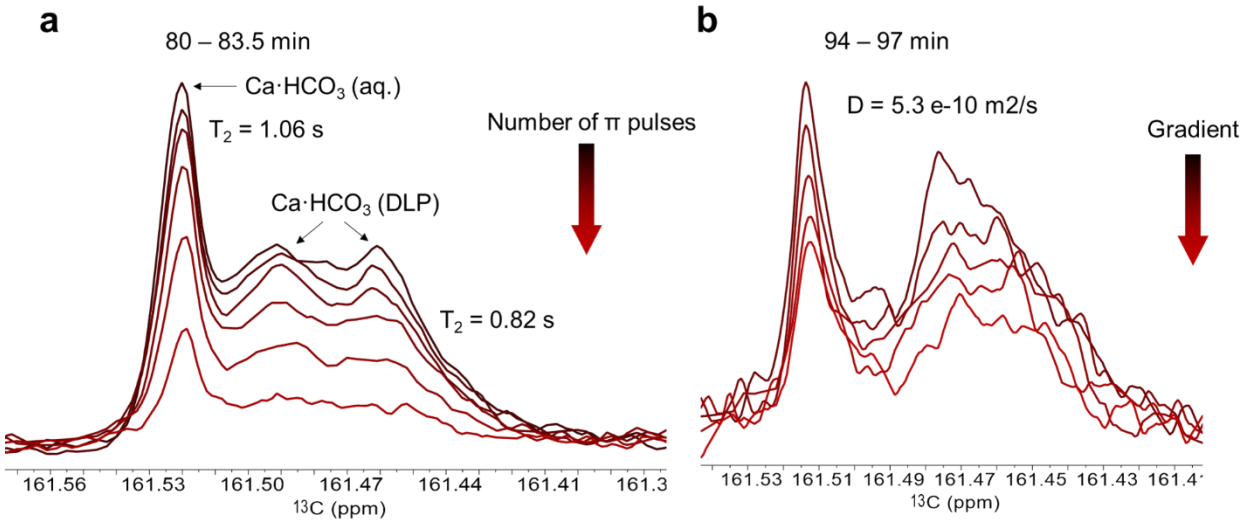

Figure S15. (a) ^{13}C NMR spectra during T_2 measurement using CPMG pulse sequence at 80 – 83.5 min after mixing 100 mM $CaCl_2$ and 100 mM $NaHCO_3$ at 5 °C. (b) ^{13}C NMR spectra during diffusion measurement using "ledbpgp2s" at 94 – 97 min.

As shown in fig. S16a, the concentration of all bicarbonate/carbonate species (the ^{13}C signals between 161.1 and 161.7 ppm, including $Ca{\cdot}HCO_3$ (DLP), $Ca{\cdot}HCO_3$ (aq.), solvated HCO_3^-, and a small amount of CO_3^{2-}), and the concentration of CO_2 estimated from ^{13}C NMR spectra are constant for about 120 min before the decomposition of $Ca{\cdot}HCO_3$ to form $CaCO_3$ and CO_2. This ~120 min is consistent with the complete disappearance of the $Ca{\cdot}HCO_3$ (aq.) signal and the broadest $Ca{\cdot}HCO_3$ (DLP) signals, indicating that the majority of $Ca{\cdot}HCO_3$ are incorporated into the DLP through diffusion and fusion of the droplets. This is similar to what we observed at 25 °C, except that a longer "incubation" time was required at a lower temperature due to the slower mobility of ions and water. ^{13}C T_2 also witnesses a rapid surge after 150 min (fig. S16b), where the broad signal sharpens and move quickly to the lower frequency, suggesting that, with decomposition of the DLP, the fraction of solvated HCO_3^- in bulk solution becomes dominant.

While $D(HCO_3^-)$ does not change as significantly as ^{13}C T_2 with time, we do observe a small decrease in $D(HCO_3^-)$ during the DLP formation period (fig. S16c). Because this decrease is relatively small (10%) compared to the experimental error (±1%), we repeated the experiments a few times and found that this decrease is real, despite being small. This is clear evidence that the DLP of $Ca{\cdot}HCO_3$ is truly a liquid, highly dynamic, but still a more condensed phase of ions than the bulk ion pairs. Here we have to emphasize the remarkable difference between the "solution-like" $D(HCO_3^-)$ observed from NMR and the "gel-like" viscosity observed from TEM. As noted above, in the TEM, the solution is placed within a thin (sub-micron) cell where the physical and chemical restriction from the solution/substrate interface unavoidably leads to exceedingly small diffusivities and an increase in viscosity of the DLP within the solution, therefore the viscosity estimated by TEM is the upper limit. On the other hand, as we mentioned before, because HCO_3^- diffuses through multiples of the characteristic length scale of the DLP and bulk solution during the NMR PFG diffusion measurements, the viscosity estimated from NMR is a lower limit.

Again, similar to our observations at 25 °C, the ^1H T_2 also experience a significant drop and a sequential rebound with time due to the involvement of water in the DLP (fig. S16d). Here, combined with the ^{13}C 1D, T_2 and diffusion results (fig. S16a-c), the pathway of $CaCO_3$ formation from $CaCl_2$ (pH 6.9) and $NaHCO_3$ (pH 8.7) solutions follows: formation of $Ca{\cdot}HCO_3$ ion pairs in bulk solution → formation of $Ca{\cdot}HCO_3$ (DLP) → decomposition of DLP to form ACC and CO_2 → releasing water from ACC dehydration. We want to mention that a similar pathway involving a liquid condensed phase (LCP) was proposed in previous work by L. Gower, et al. (Faraday Discussions, 2012, 159, 291-312), but here we show concrete evidence and details of this pathway, including the compositional evolution, the dependence on pH and the effect of additives using in-situ NMR and LP-TEM.

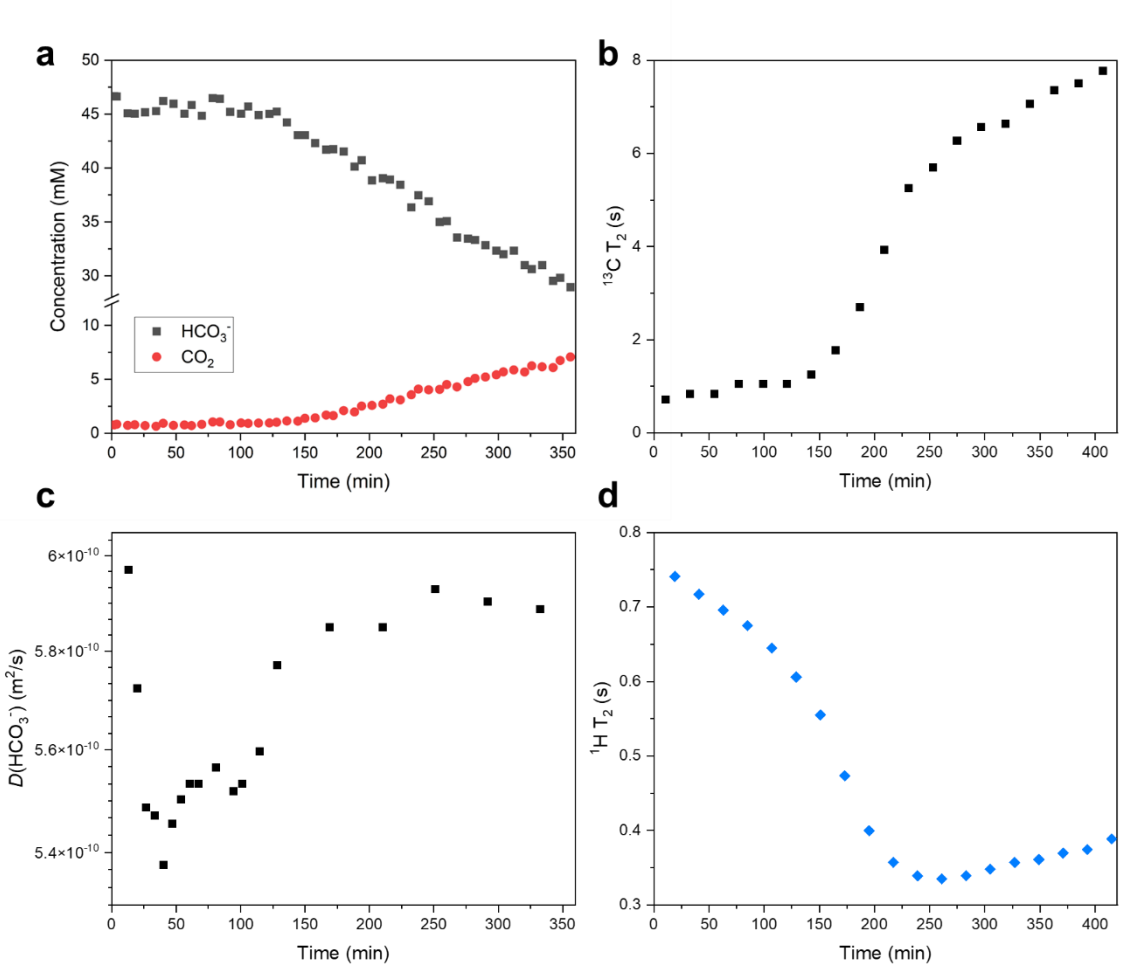

Figure S16. (a) Concentration of HCO_3^- and CO_2, (b) ^{13}C T_2 of HCO_3^-, (c) diffusion coefficient of HCO_3^-, and (d) ^1H T_2 of water plotted with time after mixing 100 mM $NaHCO_3$ and 100 mM $CaCl_2$ at 5 °C. Here (a), (b) and (d) are from one set of experiments described in Figure S12, while (c) is from another set of experiments where only ^{13}C 1D and diffusion were measured with the intention to capture the change in ^{13}C diffusion coefficient with more time points.

^{13}C NMR chemical shift analysis: $Ca{\cdot}HCO_3$ (DLP), $Ca{\cdot}HCO_3$ (aq.), free HCO_3^- and trace of $Ca{\cdot}CO_3$

The change in ^{13}C chemical shift with time can be seen in more detail at 5 °C, when the exchange between $Ca{\cdot}HCO_3$ (aq) and $Ca{\cdot}HCO_3$ (DLP) is slowed down (Fig. 2f). We can divide the reaction into three periods: $Ca{\cdot}HCO_3$ (DLP) formation during 0 – 140 min (Stage 1); DLP decomposition, fast reaction to form $CaCO_3$ and CO_2 during 140 – 230 min (Stage 2); slower decomposition reaction after 250 min (Stage 3). Here we will look into the details to see how the change in ^{13}C chemical shift can reflect these reactions.

The signal that we assigned to $Ca{\cdot}HCO_3$ (aq.) exhibits a shift from 161.58 to 161.51 ppm (the grey circles of Fig. 2f), similar to the shift from 161.51 to 161.45 ppm (the orange circles of Fig. 2f) for the signal we assigned to $Ca{\cdot}HCO_3$ (DLP) during the first 140 min. One explanation for this shift is the presence of a very small fraction of $Ca.CO_3$ ion pairs that are in fast exchange with $Ca{\cdot}HCO_3$ ion pairs (due to the fast hopping of H^+ between the ion pairs) and therefore initially visible to solution NMR, but becoming invisible (precipitating from the solution) with time. Here is our justification of this hypothesis:

In a freshly prepared $NaHCO_3$ solution, a small fraction of CO_3^{2-} (1 – 5%) is present and is in fast exchange with HCO_3^-, while the observed ^{13}C chemical shift of HCO_3^- (δ_{obs}) is the weighted average of HCO_3^- and CO_3^{2-}. So the fraction of CO_3^{2-} in the solution can be estimated by δ_{obs} using the equation below:

$$f_{\mathrm{CO_3^{2-}}} = \frac{\delta_{\mathrm{obs}} - \delta_{\mathrm{HCO_3^-}}}{\delta_{\mathrm{CO_3^{2-}}} - \delta_{\mathrm{HCO_3^-}}}$$

$\delta_{\mathrm{HCO_3^-}} = 161.082$ ppm and $\delta_{\mathrm{CO_3^{2-}}} = 169.082$ ppm were obtained at 25 °C using 50 mM $NaHCO_3$ in 10% H_2O and 90% D_2O at pH 7 and pH 14, respectively. Using ^{13}C chemical shifts, $f_{\mathrm{CO_3^{2-}}}$ can be estimated more directly and accurately than by using pH. For example, when δ_{obs}=161.283 ppm, $f_{\mathrm{CO_3^{2-}}}$=2.51%, corresponding to 1.26 mM CO_3^{2-} in the 50 mM $NaHCO_3$ solution. When δ_{obs} =161.150 ppm, $f_{\mathrm{CO_3^{2-}}}$=0.87 %, corresponding to 0.44 mM CO_3^{2-}. In both cases, we did not observe any cloudy suspension right after mixing the $NaHCO_3$ and $CaCl_2$ solutions, and the first ^{13}C signal collected 2 min after mixing was shifted to 161.575 and 161.422 ppm, respectively (fig. S17a-b). fig. S17c-d shows another two examples at 5 °C. If CO_3^{2-} immediately precipitates with Ca^{2+}, only $Ca{\cdot}HCO_3$ (DLP), $Ca{\cdot}HCO_3$ (aq.) and HCO_3^- would present in the solution, then we should observe the same chemical shift in these two mixed solutions (at around 161.4 ppm). The greater ^{13}C chemical shift after mixing with Ca^{2+} observed for a higher $f_{\mathrm{CO_3^{2-}}}$ indicates that CO_3^{2-} is also initially present in the mixed solution and is visible to solution NMR, mostly in the form of $Ca.CO_3$ ion pairs or incorporated into $Ca{\cdot}HCO_3$ (DLP). Because the level of the supersaturation is still high at 50 mM Ca^{2+} and 0.44 – 1.26 mM CO_3^{2-}, some $Ca{\cdot}CO_3$ generally precipitate either in the form of $Ca{\cdot}CO_3$ (DLP) or ACC and becomes invisible to solution NMR; this causes a shift in the ^{13}C signal to a lower frequency with time. Because the total concentration of $Ca{\cdot}CO_3$ is less than 1.5 mM, the concentration estimated from the ^{13}C HCO_3^- signal does not allow us to accurately detect this difference (especially considering the error when integrating some broad HCO_3^- signals). In other words, while the integration of ^{13}C NMR signals is not accurate enough to detect $Ca{\cdot}CO_3$, the change in ^{13}C chemical shift is easily sensitive enough to do so. Because $\delta_{\mathrm{CO_3^{2-}}} - \delta_{\mathrm{HCO_3^-}} = 8.000$ ppm and the spectral resolution of a well-defined ^{13}C signal can reach 0.1 Hz (0.0008 ppm at a magnet of 11.7 T), a change of 0.005 mM CO_3^{2-} will cause a shift of 0.1 Hz and can be seen in ^{13}C chemical shift.

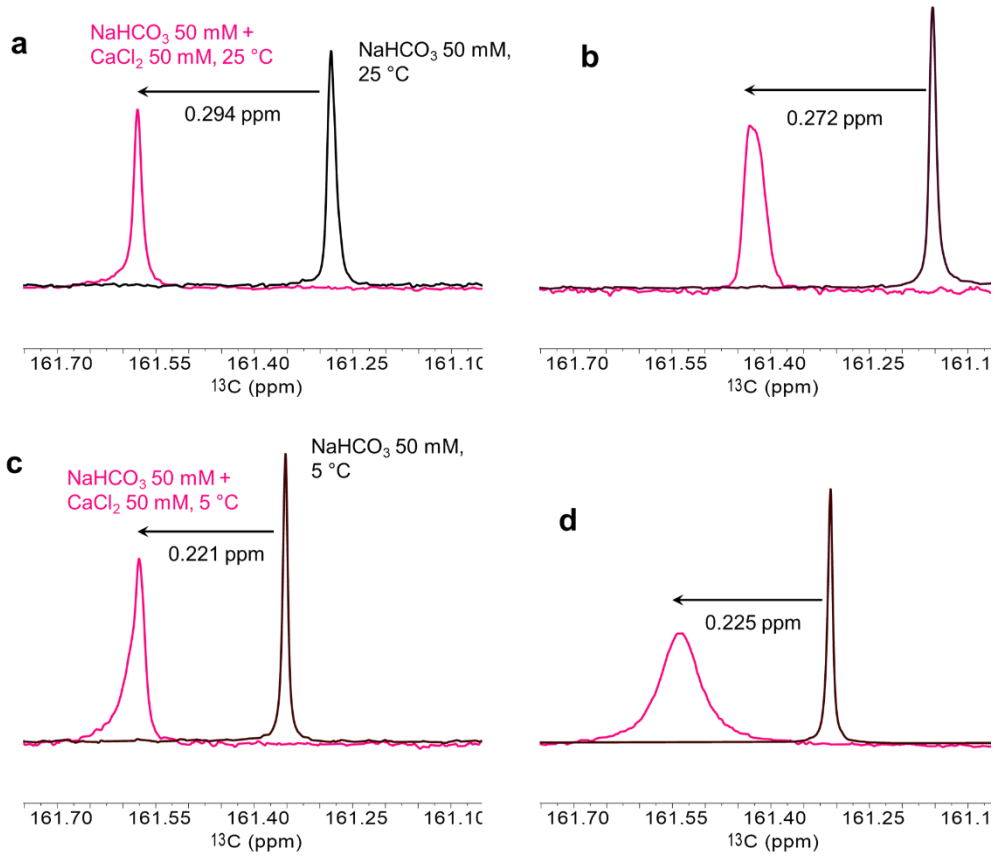

Figure S17. ^{13}C NMR spectra of 50 mM $NaHCO_3$ and the corresponding first scan (~ 2 min) of 50 mM $NaHCO_3$ and 50 mM $CaCl_2$ at 25 °C (a-b) and 5 °C (c-d). The starting solutions were prepared as 100 mM $NaHCO_3$ and 100 mM $CaCl_2$ in 10% D_2O and 90% H_2O.

With this in mind, let us look at the data in Fig. 2f. The 50 mM $NaHCO_3$ solution at 5 °C has δ_{obs}=161.352 ppm, with $\delta_{HCO_3^-} = 161.044$ ppm and $\delta_{CO_3^{2-}} = 168.847$ ppm at 5 °C, we can calculate that $f_{CO_3^{2-}}$=3.9%. After mixing $CaCl_2$ and $NaHCO_3$, the total concentration of the "HCO_3^-" is maintained at 45 – 47 mM for the first 120 min (Fig. 6A), corresponding to ~1.8 mM of CO_3^{2-}. As we mentioned before, the observed ^{13}C chemical shift decreases from161.58 to 161.51 ppm (the grey circles of Fig. 2f) and from 161.51 to 161.45 ppm (the orange circles of Fig. 2f) for the first 100 min. This 0.07 ppm change indicates a decrease of 0.90% in the fraction of CO_3^{2-}. Note that here the change of ^{13}C chemical shift in the center of gravity is from 161.58 to 161.45 ppm, this change of 0.13 ppm suggests that about half of the change in ^{13}C chemical shift can be attributed to the conversion of Ca·HCO_3 (aq) to Ca·HCO_3 (DLP), and another half to the precipitation of Ca·CO_3 over time. But due to the potential differences in ^{13}C chemical shift of Ca·HCO_3 located at different environments within the DLP, we can only roughly estimate that the decrease of Ca·CO_3 (that become invisible to solution NMR) is ~0.4 mM, which suggests that a portion of the Ca·CO_3 is still present in the Ca·HCO_3 dominated DLP. Similarly, by looking at the ^{13}C chemical shift change in Fig. 2b, we can see that the decrease in the ^{13}C chemical shift from the first scan to the point before DLP decomposition is in the range of 0.10 – 0.12 ppm for all three samples (control, with 0.4 µM DHR and with 2.5 ug/mL PAA), half of this change could arise from the conversion of Ca.HCO_3 (aq) to Ca·HCO_3 (DLP) and the other half from the precipitation of Ca·CO_3, which gives 0.3 – 0.4 mM Ca·CO_3. The additives not only stabilize the Ca·HCO_3 (DLP) but also keep Ca·CO_3 in the solution phases for a longer timer period. In addition, the decrease of pH from 7.6 to 6.9 after mixing the solutions is consistent with the reduction in the fraction of CO_3^{2-} vs HCO_3^- in the solution.
The fast decrease in ^{13}C chemical shift during 140 – 230 min is accompanied by the sharpening of the ^{13}C signals, a decrease in the total HCO_3^- concentration, and an increase in CO_2 concentration. Therefore, it is consistent with the decomposition of Ca·HCO_3 (DLP), which produces ACC, CO_2 (aq), and water, and releases some free HCO_3^- back into the solution. The relatively sharper ^{13}C signal for HCO_3^- (aq) is located at a lower frequency of Ca·HCO_3 (DLP), and we can see that briefly in Fig. 2 and fig. S12.

During Stage 3, little CO_3^{2-} is present in solution after decomposition of Ca·HCO_3 (DLP); HCO_3^- and CO_2 dominate with a small fraction of H_2CO_3. The slower decrease in the ^{13}C chemical shift can be explained by (1) the loosely associated Ca·HCO_3 turning into Ca·CO_3 and CO_2 and (2) the increasing amount of H_2CO_3. The former process is different from a system of Ca^{2+} and HCO_3^- at lower concentrations due to the presence of already dissolved CO_2; we will discuss this in more detail in a latter section. For the effect of H_2CO_3, as the concentration of CO_2 increases, the fraction of H_2CO_3 also increases. The hydration and dehydration of CO_2 can be characterized by the equilibrium constants K_H and K_D:

$$CO_2\,(aq) + H_2O \underset{k_D}{\overset{k_H}{\rightleftharpoons}} H_2CO_3$$

Here k_H and k_D are hydration and dehydration rate constants, respectively.

$$K_D = \frac{[CO_2\,(aq)]}{[H_2CO_3\,]} = \frac{k_D}{k_H}$$

At 25 °C, K_D was experimentally measured to be in the range of 720 – 930, with k_D ~ 25 – 28 s^{-1}.[14] When CO_2 reaches 10 mM in solution, the concentration of H_2CO_3 is ~12 µM.

Extrapolation of the CO_3^{2-} signal at 169.08 ppm and HCO_3^- signal at 161.08 ppm suggests that the H_2CO_3 is at about 153 ppm.[15] However, due to the small fraction of H_2CO_3 and the fast exchange between H_2CO_3 and HCO_3^-, the signal at 153 ppm is not observable, instead, the presence of H_2CO_3 will shift the ^{13}C

signal more towards the lower frequency. For example, an increase of 10 mM CO_2 (~ 12 µM) H_2CO_3 in 20 mM HCO_3^- will shift the observed $\delta(^{13}C)$ by ~0.005 ppm, which is detectable in the model high-resolution NMR spectra.

In summary, the evolution of the chemical shifts summarized in Fig. 2f is consistent with the reaction pathway that we concluded in the previous section and Fig. 4 of the main text.

Effect of dissolved CO_2 and resultant low pH on ion pairing of $Ca{\cdot}HCO_3$

The remaining question during the ^{13}C NMR spectral monitoring of the nucleation process is that why the relatively highly concentrated ions of HCO_3^- and Ca^{2+} left in the solution by the end of DLP decomposition do not coordinate again into ion pairs and resume the $Ca{\cdot}HCO_3$ (aq) → $Ca{\cdot}HCO_3$ (DLP) process again. For example, at 25 °C, the observed ^{13}C chemical shift is 161.188 ppm at 30 min, appearing as a very broad signal, which we attributed to the dominating $Ca{\cdot}HCO_3$ (DLP). The DLP decomposition occurs during ~20 – 60 min and, at 60 min, the ^{13}C chemical shift is 161.121 ppm, which is still not that of pure HCO_3^- (aq), which is at 161.082 ppm. At 100 min after the reaction, the remaining HCO_3^- in the solution is about 25 mM, and the remaining Ca^{2+} should be around 37.5 mM as the dominant reaction uses 1 Ca^{2+} and 2 HCO_3^-. With the many Ca^{2+} and HCO_3^- ions available, we expect them to form $Ca{\cdot}HCO_3$ (aq) or $Ca{\cdot}HCO_3$ (DLP). Instead, we detect a sharp ^{13}C signal that is only 0.04 ppm away from the free HCO_3^- signal. The main reason why these Ca and HCO_3 ions do not associate by the end of the DLP decomposition stage is the presence of a large amount of dissolved CO_2 and resultant low pH in the solution. Here we show a few more new experiments to justify this conclusion.

(1) We mixed 50 mM $CaCl_2$ and 50 mM $NaHCO_3$ (25 mM for both Ca^{2+} and HCO_3^- after mixing), and we did observe the initial shift of 0.252 ppm in ^{13}C NMR to a higher frequency from what is seen in the original $NaHCO_3$ solution (fig. S18) and the HCO_3^- signal goes through the broadening and sharpening process coupled with CO_2 generation, similar to what we detected in 100 mM solutions. We do notice some differences between the 25 mM and 50 mM $Ca{\cdot}HCO_3$ solutions in the dependence of the spectral behavior on time, but this will be a topic for our future studies about the effect of ion concentrations on DLP formation and transformation. For this paper, the observed initial ^{13}C chemical shift suggests that the strong coordination between Ca^{2+} and HCO_3^- is still present at a lower concentration, as we expected. So the concentration is not the issue, the main differences that remains are that the solution after DLP decomposition has about 10 mM dissolved CO_2 and the resultant low pH (pH ~ 6.7 after 100 min of reaction and 6.3 after 12 hours).

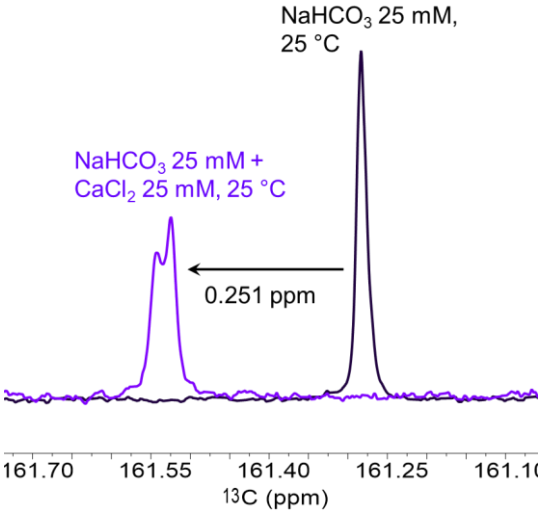

Figure S18. ^{13}C spectrum of fresh prepared 25 mM $NaHCO_3$ at 25 °C (black line) compared to the first spectrum collected 2 min after mixing fresh-prepared 50 mM $NaHCO_3$ and 50 mM $CaCl_2$ in 90% H_2O and 10% D_2O (25 mM Ca^{2+} and HCO_3^- after mixing).

(2) In order to check the effect of dissolved CO_2 on the ion paring between Ca^{2+} and HCO_3^-, we added CO_2 directly to 100 mM solutions before mixing them. In this experiment, we bubbled ^{13}C-labled CO_2 (32 psi) into an NMR tube filled with 250 μL $NaHCO_3$ (100 mM) for one minute, then added 250 μL $CaCl_2$ (100 mM) to the NMR tube with the CO_2 bubbling continuing for another minute. We then slowly took the CO_2 tubing out from the NMR tube before capping to ensure that the empty space of the NMR tube is backfilled with 1 atm CO_2. The first ^{13}C spectrum taken at 5 minutes after mixing the two solutions is shown in fig. S19. Surprisingly, the HCO_3^- signal is located at the 161.091 ppm, which is very close to the signal of free HCO_3^-. The concentration of CO_2 estimated from the integration ratio between the two signals is 35.5 mM. This is consistent with the CO_2 solubility in pure water, which is 0.59×10^{-3} molar fraction at 0.996 atm and 25 °C,[16] corresponding to 32.8 mM. pH of this solution is 6.6. This observation suggests that the presence of dissolved CO_2 or the resultant low pH highly inhibits the coordination between Ca^{2+} and HCO_3^-.

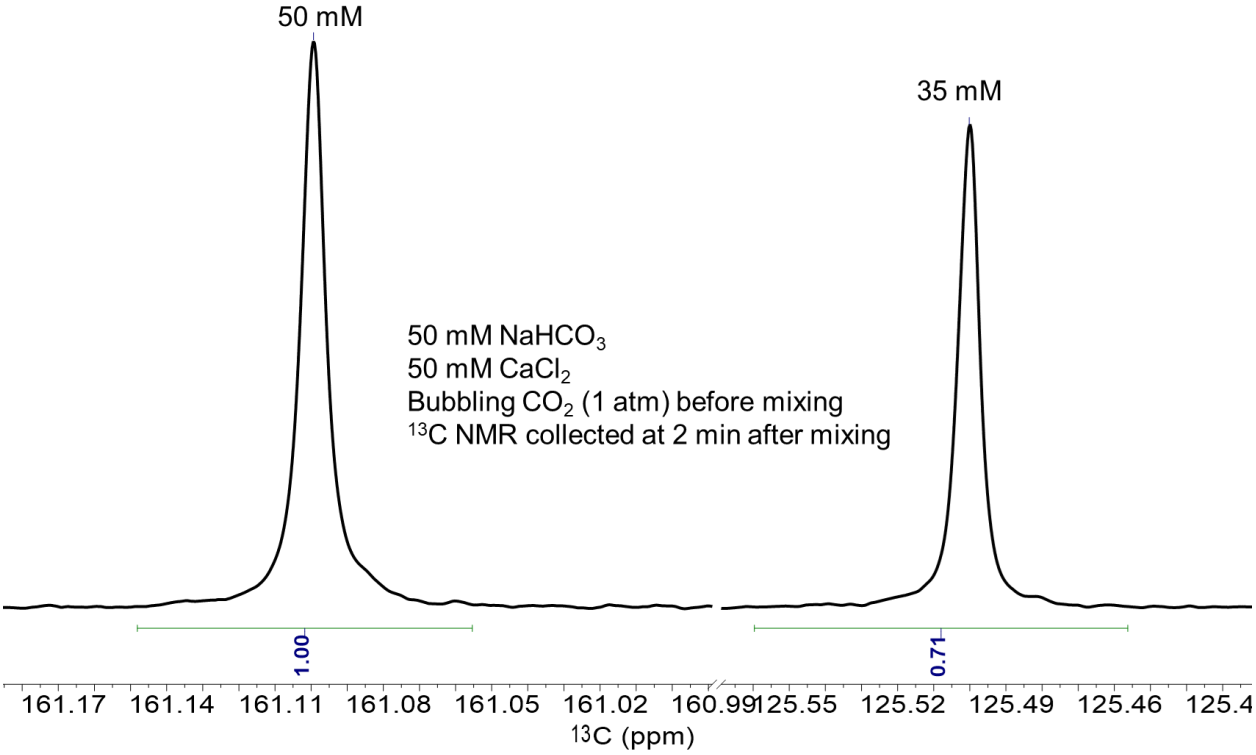

Figure S19. ^{13}C spectrum collected 5 min after mixing 100 $NaHCO_3$ and 100 mM $CaCl_2$ solutions with saturated CO_2.

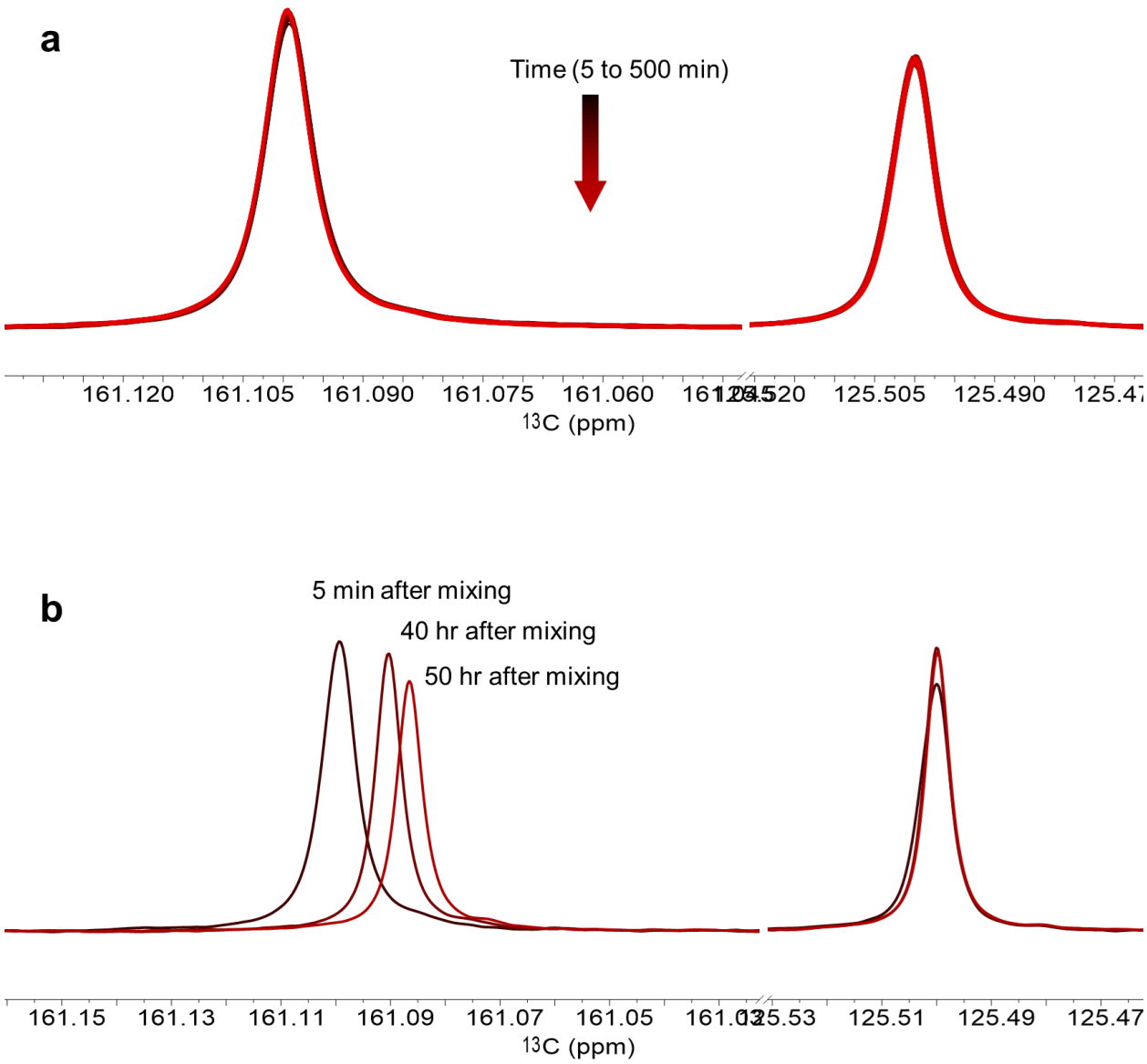

Figure S20. ^{13}C spectra collected after mixing 100 $NaHCO_3$ and 100 mM $CaCl_2$ solutions with saturated CO_2: (a) 5 – 500 min; (b) comparison between 5 min, 40 hr and 50 hr after mixing.

This mixed solution with saturated CO_2 was monitored for 50 hours. ^{13}C spectra of the first 500 min do not show obvious changes (fig. S20a). But with time, the HCO_3^- signal slowly shifts to lower frequency with a reduced intensity. We observe some white crystals at the bottom of the NMR tube at 50 hours, and the ^{13}C signal shifts -0.013 ppm with a reduced concentration from 50.0 to 34.2 mM, while the CO_2 concentration is mostly unaltered (fig. S20b). Here CO_2 may escape into the gas phase and out of the NMR tube (which is capped but not sealed) because the dissolved CO_2 already reaches the solubility limit. By comparison, it takes only ~60 min for the mixed solution without CO_2 to show a reduction in HCO_3- concentration from 45 to 30 mM (Fig. 2c). This observation suggests the accumulated dissolved CO_2 or

the resultant low pH can significantly slow down the decomposition reaction $Ca(HCO_3)_2 \rightarrow CaCO_3 + CO_2$ by interfering with ion pairing between Ca^{2+} and HCO_3^-.

(3) In order to check whether the effect of CO_2 is reversable, we took the NMR tube out at 50 hr and bubbled N_2 to the solution for 5 min with the intention of removing the CO_2. Indeed, the first ^{13}C spectrum taken (at 5 min after bubbling N_2, pH 8.7) shows that the HCO_3^- and CO_2 concentrations decreased to 19.9 mM and 0.3 mM, respectively. More importantly, the HCO_3^- signal in the first ^{13}C spectrum is located at 161.21 ppm (shifted from 161.09 ppm in the presence of CO_2), and it goes through a broadening/sharpening process again with a rapid increase in the CO_2 signal, indicating that the ion paring between Ca and HCO_3^- returns after the CO_2 is removed.

(4) Because the solution pH changes with the concentration of dissolved CO_2, in order to identify if the CO_2 or pH plays the main role, we used HEPES buffer solution, which is known for maintaining physiological pH despite the changes in CO_2 concentration. In this experiment, ^{13}C CO_2 was introduced to a solution of 50 mM $CaCl_2$ and 50 mM HEPES at pH 7.7, ^{13}C NMR spectra were collected every 5 min after CO_2 introduction. The first spectrum showed that HCO_3^- was generated from CO_2 hydration with a concentration of 30 mM and a chemical shift of 161.241 ppm, while CO_2 had a concentration of 18 mM. pH of the solution was 7.2. The HCO_3^- signal again went through a broadening/sharpening process, with a decrease of 16 mM in HCO_3^- concentration and an increase of 8 mM in CO_2 concentration after 300 min. In contrast, for a solution of 50 mM $CaCl_2$ at pH 7.7 without a buffer, pH dropped to 4.5 with saturated CO_2, and no $CaCO_3$ precipitation was observed even after 3 months. Therefore, it is clear that the low pH plays a more critical role in interfering with the Ca^{2+} and HCO_3^- ion pairing than the CO_2 concentration.

Because the deprotonation of HCO_3^- is slowed down due to the additional H^+ in solution and because deprotonation of HCO_3^- is required to transit from $Ca{\cdot}HCO_3$ DLP to $Ca{\cdot}CO_3$ ACC, we would expect that the additional H^+ would slow down the transformation rate from DLP to solid. Furthermore, the supersaturation becomes much lower at pH < 7 with a fraction of $CO_3^{2-} < 10^{-4}$. Nevertheless, it is surprising that the additional H^+ also disturbs the initial steps of $CaCO_3$ nucleation: the ion pairing between Ca^{2+} and HCO_3^- and the subsequent formation of $Ca{\cdot}HCO_3$ DLP. This interference may occur due to the competition between Ca^{2+} and H^+ to coordinate to HCO_3^-. The dynamic balance between $CO_2 + H_2O \leftrightarrow H_2CO_3 \leftrightarrow H^+ + HCO_3^-$ may significantly reduce the charge density of HCO_3^-, lowering the chance of ion pairing between Ca^{2+} and HCO_3^-. Thus, the single-line ^{13}C signal after DLP decomposition (eg. at 161.121 ppm after 60 min) is the result of HCO_3^- exchanging between partially associated $Ca{\cdot}HCO_3$ ion pairs and free HCO_3^- ions at low pH. Note that here we use "partially associated $Ca{\cdot}HCO_3$" to distinguish this species at low pH due to the presence of a large fraction of dissolved CO_2, from the more tightly coordinated $Ca{\cdot}HCO_3$ (aq) whose signals are shifted ~0.3 ppm from the original HCO_3^- in the absence of CO_2.

In conclusion, the low pH as a result of dissolved CO_2 generated from the decomposition of $Ca{\cdot}HCO_3$ (DLP) is an inhibitor of ion paring between Ca^{2+} and HCO_3^-. We do not yet know the exact concentration of dissolved CO_2 or the precise pH level that begins to affect ion pairing and DLP formation, but we are confident that the main conclusion of our paper – $Ca{\cdot}HCO_3$ DLP formation followed by decomposition to $CaCO_3$ ACC and CO_2 – remains unchanged, because the amount of CO_2 is less than 2 mM with pH ~ 7 before the onset of DLP decomposition. In addition, the effect of dissolved CO_2 on the reaction rate and even mechanism highlights the importance of whether and how quickly CO_2 can be removed from the reaction solution. This self-restricting process unless CO_2 is removed is also relevant to geochemical settings, for example, as previously reported, the conversion to CO_2 is a rate limiting step in calcite precipitation, depending on the volume to area ratio of the minerals.[17,18] Another example is the formation of speleothems. As the mineral calcite being dissolved from limestone rocks into the acidic water of CO_2

and carbonic acid, Ca^{2+} and HCO_3^- can coexist as loosely coordinating ion pairs with CO_2 at relatively high concentrations (low pH), once this water flow gets exposed to air during dripping or encountering other surfaces, a portion of CO_2 can evaporate to air, then DLP formation and decomposition to ACC may occur immediately afterwards to create speleothems. Because ACC formation is always accompanied by CO_2 generation when the starting solutions are acidic (bicarbonate, carbonic acid, and CO_2), the removal of CO_2 is always critical for the reaction to continue. This is why the higher surface to volume ratio the flowing water experiences; the faster CO_2 may be removed and ACC may be formed. In addition, now we can see that another major difference between TEM and NMR experiments is that, although the solution in a TEM cell has a much higher surface to volume ratio than the solution in a NMR tube, TEM cell is hermetically sealed, preventing CO_2 escape; whereas the dissolved CO_2 can exchange slowly with the atmosphere in a capped (not sealed) NMR tube.

Effect of additives on the ^{13}C NMR lineshapes

While the single-line ^{13}C signal is dominating after DLP decomposition in the presence of dissolved CO_2 for the control samples at both 25 °C and 5 °C, two distinguishable signals are present with the addition of 0.6 µM DHR49-Neg, As shown in fig. S21 (a portion of which is shown in Fig. 2g), a relatively sharp signal located at a lower frequency appears after 80 min (marked in green), along with the onset of fast growth in CO_2 (marked in orange). The relatively sharp signal has a longer ^{13}C T_2 than the broader signal (fig. S22), suggesting a faster reorientation motion. Here we assign this signal as bulk HCO_3^- as a result of the exchanging between free (fully solvated) HCO_3^- and partially associated $Ca{\cdot}HCO_3$ ion pairs in bulk in the presence of a relatively large fraction of CO_2 (> 5 mM). The relatively broader signal during DLP decomposition is also not the same as the much broader signal during DLP formation, as the DLP size and shape would have changed with decomposition. The large fraction of dissolved CO_2 may also affect the DLP structure and dynamics. Nevertheless, the growth of the sharper bulk HCO_3^- signal and CO_2 at the expense of the broader $Ca{\cdot}HCO_3$ (DLP) signal is consistent with our hypothesized pathway in Fig. 4.

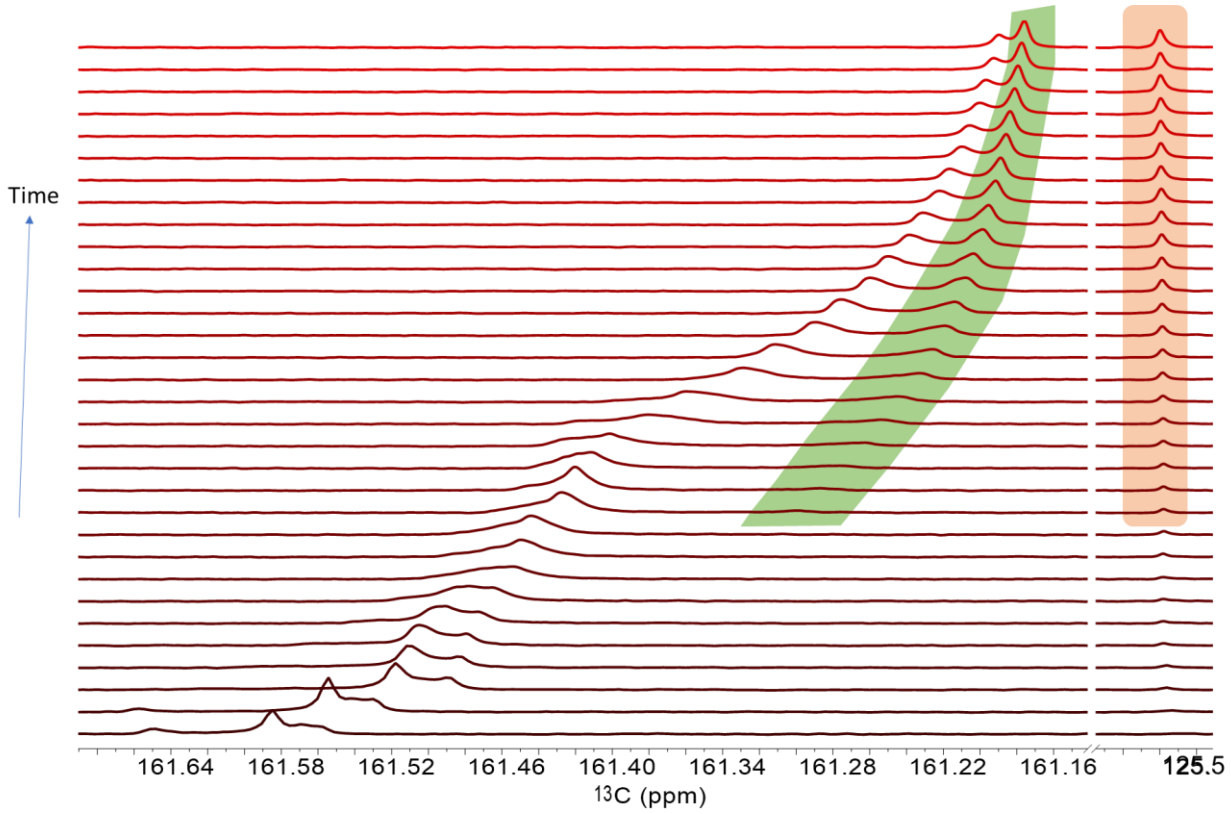

Figure S21. ^{13}C spectra collected at 25 °C after mixing fresh-prepared 100 mM $NaHCO_3$ (pH 8.7) and 100 mM $CaCl_2$ (pH 6.9) with 1.2 µM DHR49-Neg in 90% H_2O and 10% D_2O.

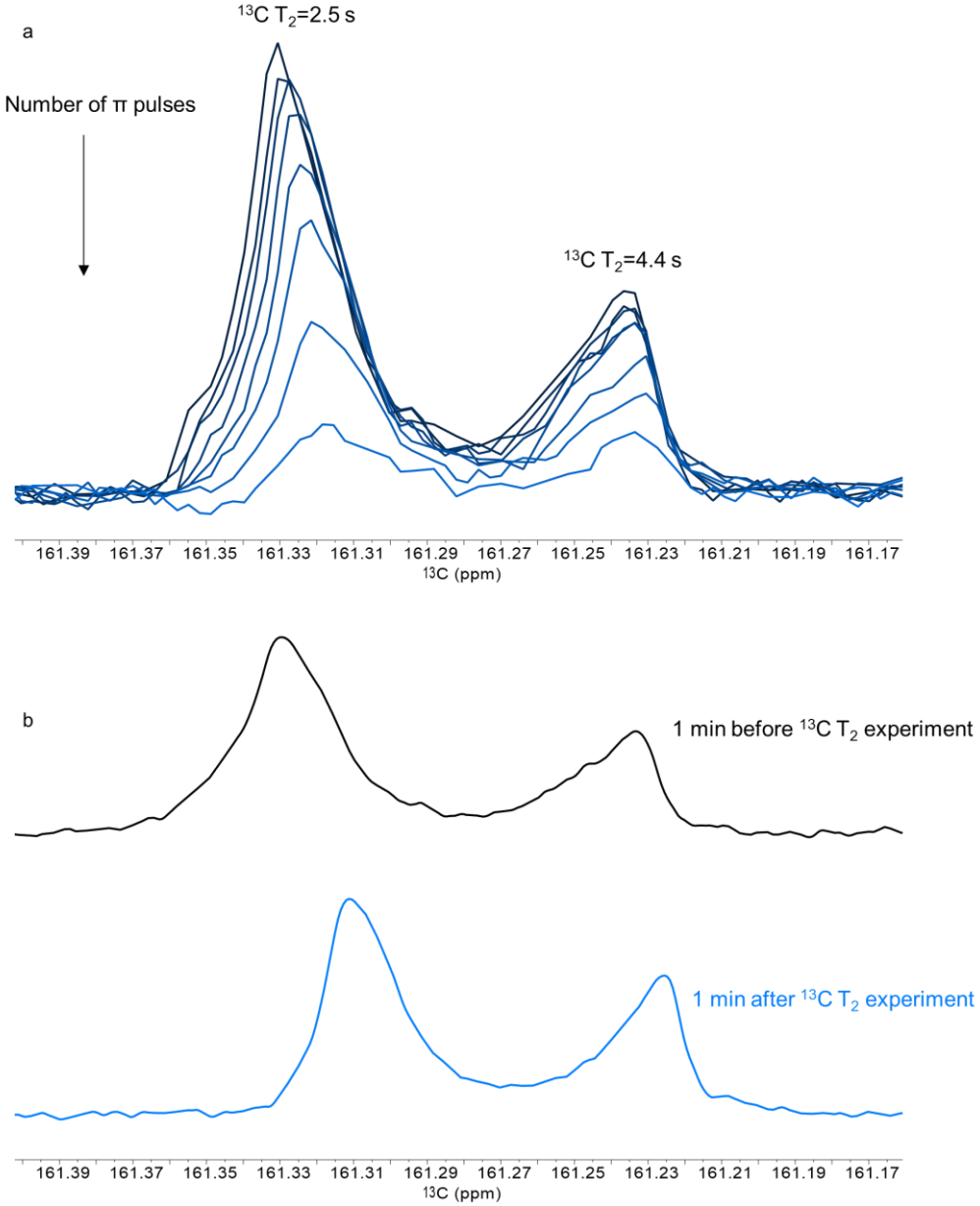

Figure S22. (a) ^{13}C spectra during T_2 measurement at 132 min after mixing fresh-prepared 100 mM $NaHCO_3$ (pH 8.7) and 100 mM $CaCl_2$ (pH 6.9) with 1.2 µM DHR49-Neg in 90% H_2O and 10% D_2O. (b) ^{13}C single-pulse spectra before and after the T_2 measurements show that the change in the T_2 measurements is not caused by the reaction with time.

Similar pattern is observed in bovine serum albumin (BSA) as another additive (5.5 µM in 100 mM $CaCl_2$), as shown in fig. S23. The DLP stabilization time is increased from 30 min to 50 min with 2.75 µM BSA, which is similar to the effect of 0.4 µM DHR49-Neg. The much longer time before ^1H T_2 rebounds (200 min for 2.75 µM BSA compared to 70 min for 0.4 µM DHR49-Neg) suggested that more water is involved in the DLP formation with 2.75 µM BSA. The stabilization effect of a native protein such as BSA at a higher concentration is comparable to the specially designed protein DHR49-Neg at a lower concentration.

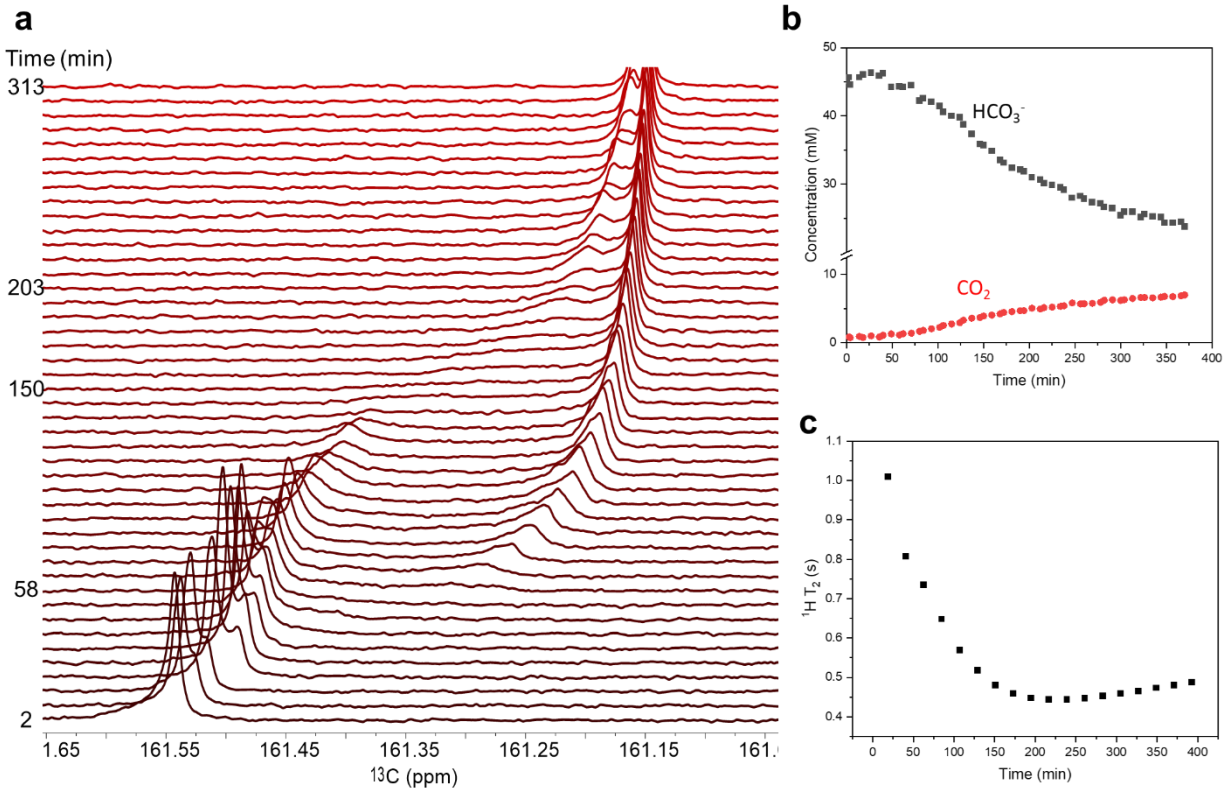

Figure S23. (a) ^{13}C spectra collected at 25 °C after mixing fresh-prepared 100 mM $NaHCO_3$ (pH 8.7) and 100 mM $CaCl_2$ (pH 6.9) with 5.5 µM BSA in 90% H_2O and 10% D_2O. (b) Concentration of HCO_3^- and CO_2 estimated from ^{13}C spectra and (c) ^1H T_2 of water plotted as a function of time.

In some scenarios, we can estimate the populations of $Ca{\cdot}HCO_3$ (aq), $Ca{\cdot}HCO_3$ (DLP) and bulk HCO_3^- when the exchange rates between them are adequately slowed down. For example, as shown in fig. S12 and S13, where $Ca{\cdot}HCO_3$ (aq) and $Ca{\cdot}HCO_3$ (DLP) exhibit distinguishable ^{13}C chemical signals due to the slower exchange between them at a lower temperature (~5 °C), we can calculate the fraction of each species after line fitting (fig. S24a). Note that in this way, because the fraction of CO_3^{2-} is very small and can be neglected during our analysis as we are not using weighted averaging ^{13}C chemical shift for population estimation. On the other hand, as shown in fig. S21, where $Ca{\cdot}HCO_3$ (DLP) and bulk HCO_3^- exhibit distinguishable ^{13}C chemical shifts as the additive DHR49-Neg slows down the exchange between these two species, we can estimate the fraction of each from line fitting (fig. S24b).

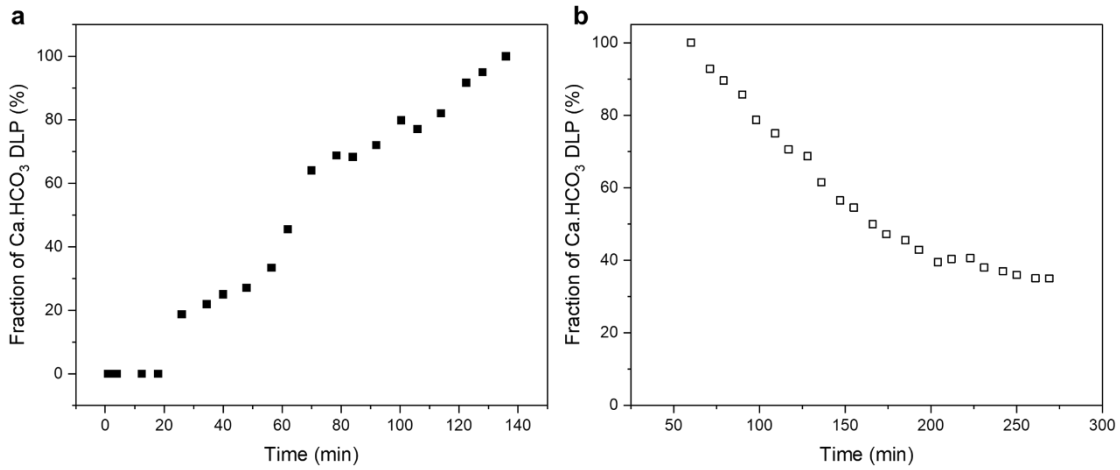

Figure S24 (a) The fraction of $Ca{\cdot}HCO_3$ (DLP) increases with time at the expense of $Ca{\cdot}HCO_3$ (aq) after mixing 100 mM $NaHCO_3$ and 100 mM $CaCl_2$ at 5 °C, corresponding to fig. S12 and S13. (b) The fraction of $Ca{\cdot}HCO_3$ (DLP) decreases with time accompanied by the increases in bulk HCO_3^- starting from 50 min after mixing 100 mM $NaHCO_3$, 100 mM $CaCl_2$ and 1.2 μM DHR49-Neg at 25 °C, corresponding to fig. S21.

When DHR49-Neg and PAA were used at concentrations giving comparable numbers of carboxyl groups — e.g., 0.4 μM DHR49-Neg (~28 μM COOH) vs. 2.5 μg/mL 1.8 kDa PAA (~35 μM COOH) — the results show that PAA is more effective at DLP stabilization (fig. S25 - S26, Fig. 2b-e).

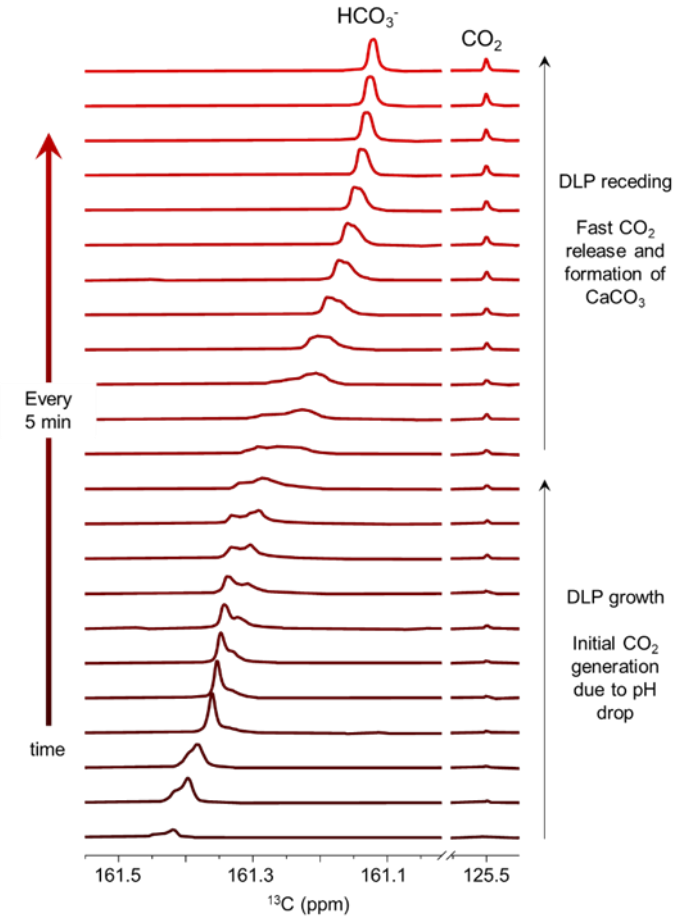

Figure S25. Time dependent ^{13}C NMR spectra after mixing 100 mM $NaHCO_3$ with 0.8 μM DHR49-Neg (pH 8.7) and 100 mM $CaCl_2$ (pH 6.9).

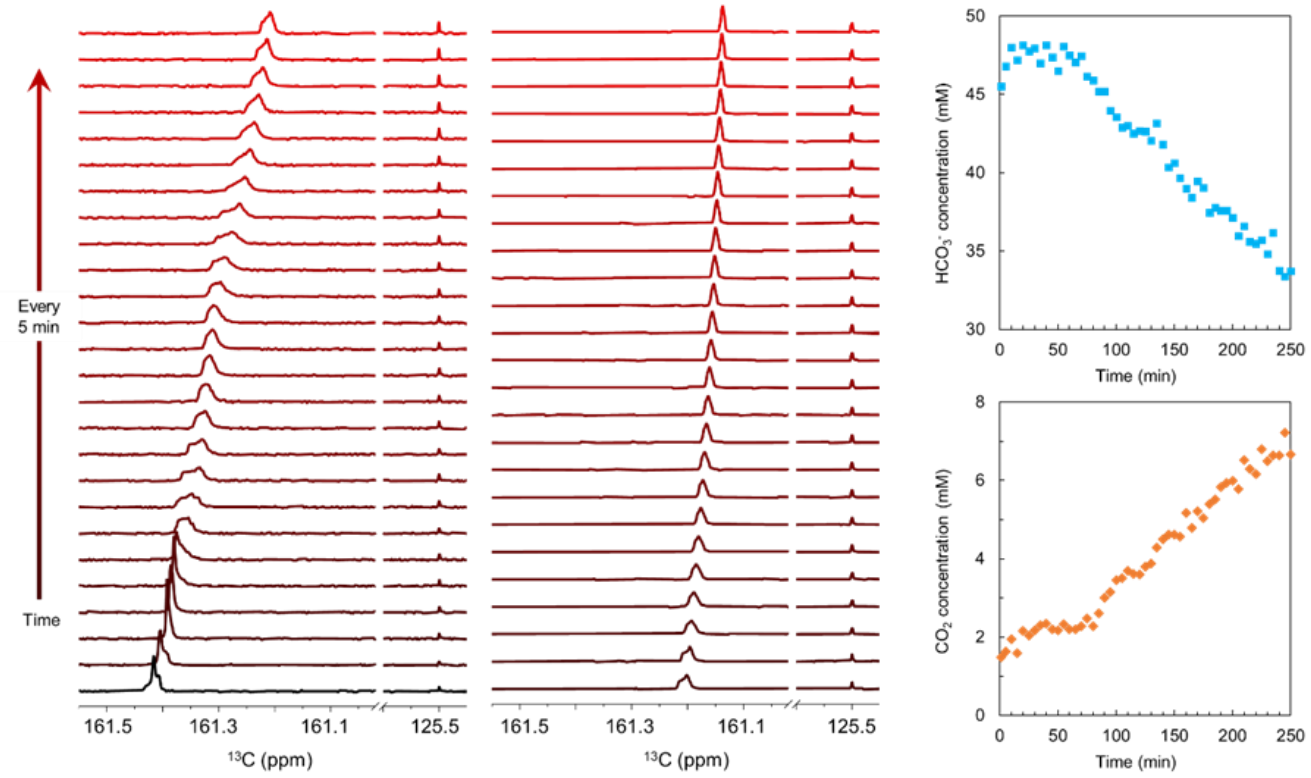

Figure S26. Time dependent ^{13}C NMR spectra and the changes of HCO_3^- and CO_2 concentration within 250 min after mixing 100 mM $NaHCO_3$ with 5.0 μg/mL 1.8 kDa PAA (pH 8.7) and 100 mM $CaCl_2$ (pH 6.9).

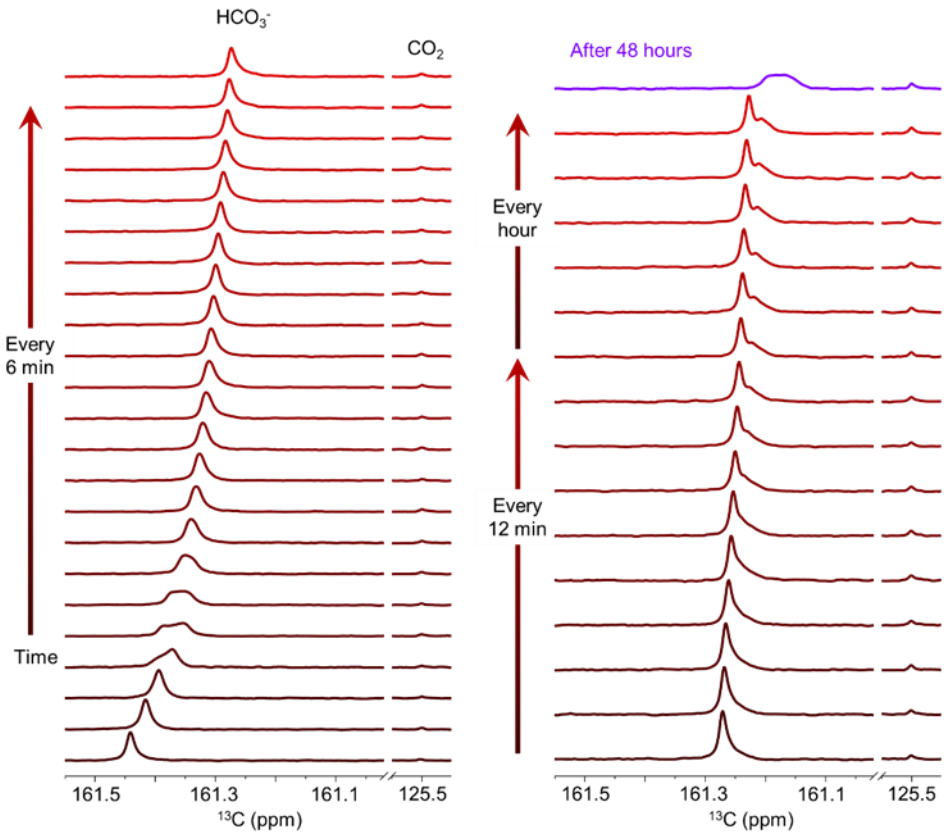

Figure S27. Time dependent ^{13}C NMR spectra and the changes of HCO_3^- and CO_2 concentration within 250 min after mixing 100 mM $NaHCO_3$ with 50 μg/mL 1.8 kDa PAA (pH 8.7) and 100 mM $CaCl_2$ (pH 6.9).

While the ^{13}C NMR lineshape analysis allows for monitoring speciation changes during nucleation, it is important that we do not overinterpret the results due to the complicated and ever-changing environment over the entire nucleation process. The heterogenous environment of the reaction solution which consists of liquid, dissolved CO_2, DLP, and precipitating ACC may lead to inadequate shimming during NMR acquisitions, and therefore yielding splitting in ^{13}C spectra caused by the overall heterogeneity of the solution. For example, in fig. S23, with the addition of 2.75 μM BSA, the small splitting in the initial few spectra may be caused by the artificial effect of the poor shimming. As shown in fig. S28a, the ^{13}C T_2 measurements show that all peaks decay at a similar rate (exhibit a similar T_2), indicating that these signals arise from the same or similar local environments. Especially with a separation of only 0.03 ppm in chemical shift for all these signals, we can attribute these signals to either similar species with slightly different environments or the same species with an artificial lineshape due to inadequate shimming. We cannot distinguish between these two cases. This type of small splitting in the first few ^{13}C spectra after mixing is commonly seen in all the solutions with or without additives.; these spectra have many different variations and do not have a clear pattern in changes with time. Thus, we do not want to overinterpret the data because they may be artificial or insignificant.

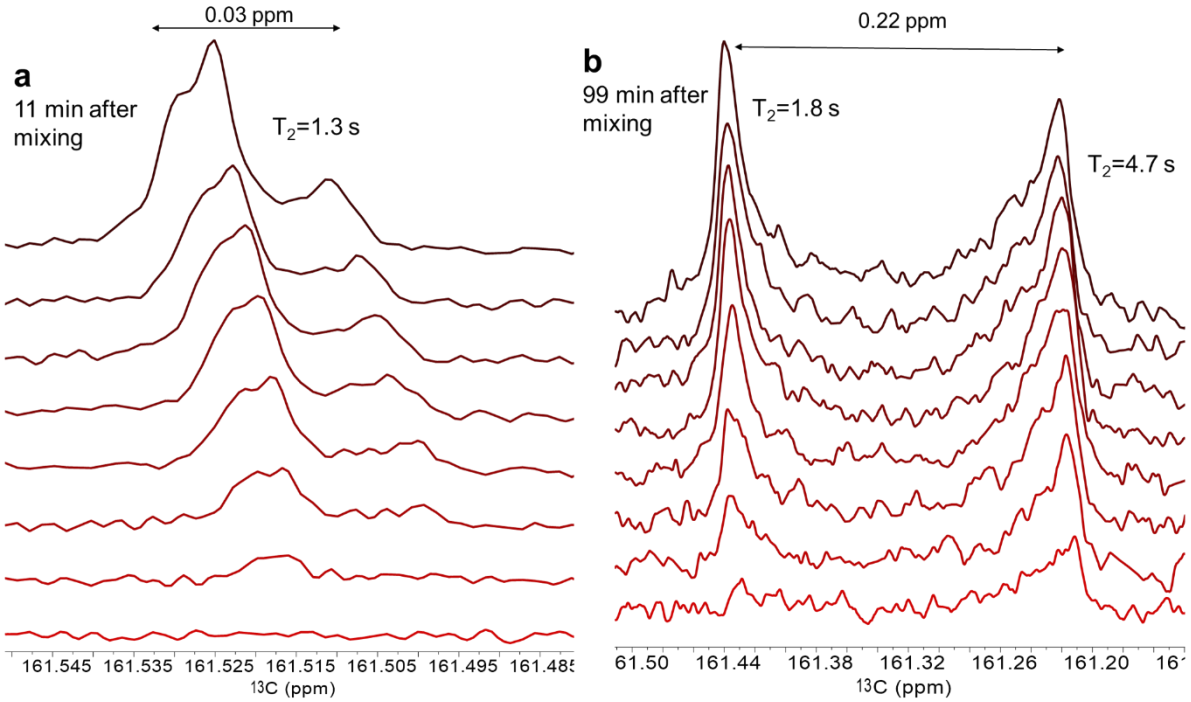

Figure S28. ^{13}C NMR spectra during T_2 measurements at 11 min (a) and 99 min (b) after mixing the fresh-prepared 100 mM $NaHCO_3$ (pH 8.7) and 100 mM $CaCl_2$ (pH 6.9) with 5.5 μM BSA in 90% H_2O and 10% D_2O.

On the other hand, the relatively larger splitting in the later spectra reflect the conversion between the two species (DLP and bulk HCO_3^-). As shown in fig. S22 and fig. S28b, ^{13}C T_2 measurements clearly show that the signal at a higher frequency has a shorter T_2 than the signal at a lower frequency, which is consistent with our assignment that HCO_3^- within DLP has a shorter T_2 than bulk HCO_3^- due to the confinement of DLP. The 0.22 ppm difference in the chemical shift is also sufficient to manifest the different local electronic environment experienced by the different HCO_3^- species. Therefore, this type of splitting can be used to understand the transition from $Ca{\cdot}HCO_3^-$ ion pairs in solution to $Ca{\cdot}HCO_3^-$ (DLP), then from DLP to bulk HCO_3^- as we have demonstrated in the previous sections.

However, there is still some significant difference in the NMR spectra of the control and different additives that is reproducible in different trials, but has not been discussed yet. By comparing the few broadest spectra in Fig. 2a (control), fig. S21 and S25 (DHR-Neg49), and fig. S26 and S27 (PAA), and also in fig. S31 (control, high pH) and fig. S32-33 (DHR-Neg, high pH), a general trend that emerges is that the spectra of DLP are broader with DHR, but are sharper in the presence of PAA (fig. S29). The ^{13}C linewidth is affected by the distribution of and exchange between multiple sites, chemical shift anisotropy, and dipole-dipole interactions, which are modulated by reorientation motion of carbon. Therefore, this trend could have three possible explanations: (1) DHR-Neg increases the distribution of $Ca{\cdot}HCO_3^-$ local environments within the DLP (i.e., a more heterogenous DLP), while PAA decreases this distribution (i.e., more homogenous DLP); (2) mobility of $Ca{\cdot}HCO_3^-$ (DLP) is slower with DHR-Neg but faster with PAA; or (3) exchange between HCO_3^- sites is slower with DHR-Neg but faster with PAA. Further experiments at varying temperatures and concentrations with the assistance of molecular modeling may help identify the difference effects of additives during $CaCO_3$ nucleation.

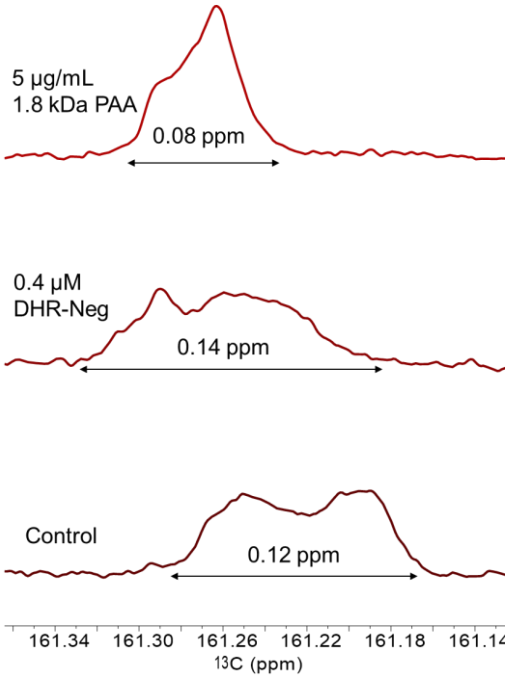

Figure S29. The ^{13}C spectra right before DLP decomposition in Fig. 2a (control), fig. S25 (DHR-Neg), and fig. S26 (1.8 kDa PAA).

Evidence implies the formation of DLP at an early stage

We initiated the precipitation reaction by mixing 100 mM $CaCl_2$ and 100 mM $NaHCO_3$ solution. Initially, a highly supersaturated $Ca(HCO_3)_2$ solution was separated into an emulsion, presumably amorphous DLP, as illustrated by in situ liquid ATR-FTIR (fig. S30). The presence of a broad peak at ~1640 cm^{-1} may be attributed to the existence of HCO_3^- and H_2O, implying the formation of DLP containing HCO_3^- and H_2O. As a control experiment, when 100 mM $NaHCO_3$ was replaced by 100 mM Na_2CO_3, the quick formation of calcite was observed by in situ ATR-FTIR (fig. S30b). In addition, ex situ TEM investigations show the existence of an amorphous DLP precursor: the obvious wetting behavior (fig. S2a), the presence of continuous amorphous (fig. S2b-c) and vaterite films (fig. S2d), and round amorphous particle with low contrast in Cryo-TEM image (fig. S2e).

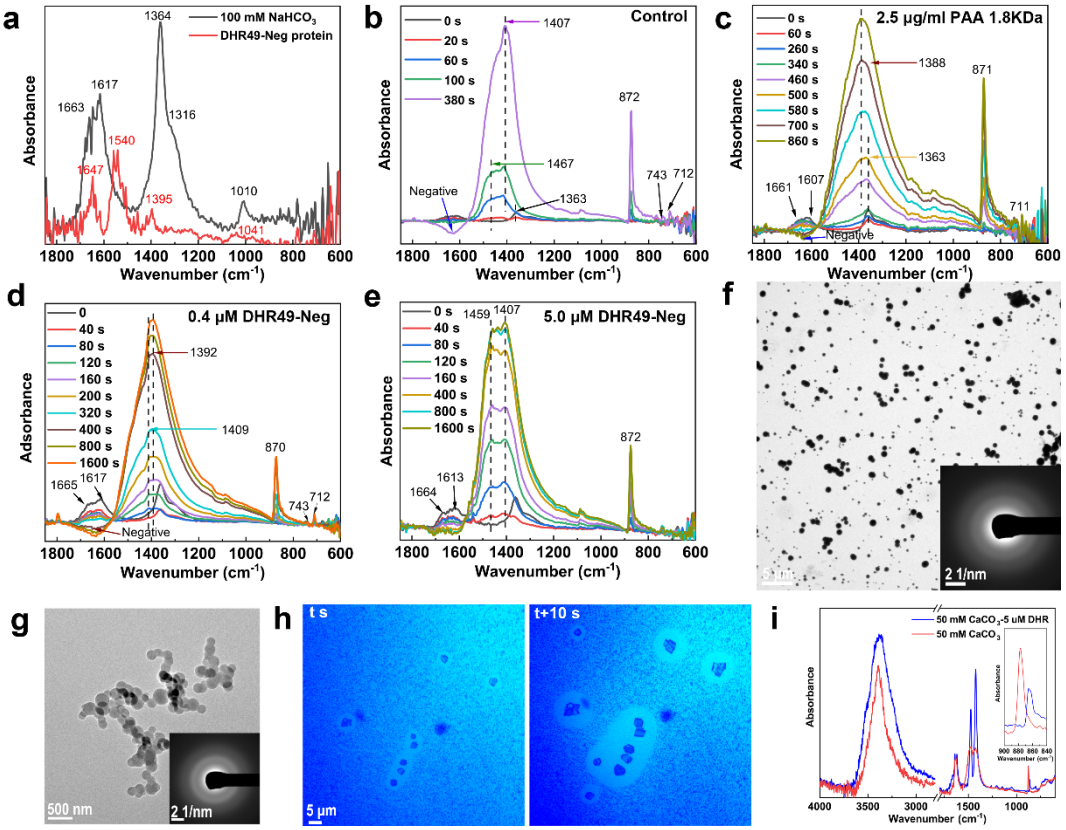

Figure S30. The formation and evolution process of DLP under a range of conditions. (a) ATR-FTIR spectra of 100 mM $NaHCO_3$ and 54 μM DHR49-Neg protein solutions (no $CaCl_2$ added). (b-e) Time-dependent ATR-FTIR analyses using 50 mM $NaHCO_3$ and $CaCl_2$ as precursors with H_2O as background without additives (b), in the presence of 2.5 μg/ml 1.8 KDa PAA (c), 0.4 μM DHR49-Neg (d) and 5.0 μM DHR49-Neg protein (e). Because the background signal from the H_2O bending vibration was subtracted, the positive broad peak between 1600-1670 cm^{-1} should be from HCO_3^- in the $HCO_3^-(H_2O)_n$ accumulated at the ATR prism-solution interface. The broad peak decreases to negative vales with time as amorphous or crystalline $CaCO_3$ solid forms and precipitates onto the prism, thereby replacing water molecules. Therefore, we speculate that the positive peak reflects formation of highly hydrated DLP. The broad asymmetric peak due to CO_3^2stretching at 1388-1470 cm^{-1} is initially split and sharpens at 100 - 380 s in the absence of protein concomitant with decreasing HCO_3^- and water vibrational strength. This result is consistent with a solidification process of DLP (split peak) into ACC (broad peak) and final evolution into

calcite (sharp peak). Comparing the peak for the asymmetric stretch of HCO_3^- in the different conditions, we hypothesize that the DLP exists in the initial 100 s (b), 580 s (c), 320 s (d), and 1600 s (e), respectively. (f) TEM image shows the amorphous particles at 25 mins in the presence of 5 μM DHR49-Neg protein. (g) TEM and corresponding SAED images show the ACC particles without additives. (h) Time-dependent optical microscopy image sequences show the dissolution and recrystallization of ACC into calcite in the additive-free control experiments. (i) The ATR-FTIR results with pure $CaCO_3$ and $CaCO_3$ with 5 μM DHR49-Neg protein.

In-situ solution NMR monitoring of multi-step composite DLP formation and transformation at higher pH

To determine whether an equivalent pathway involving a $CaCO_3$ DLP can arise, we increased the solution pH and thereby the ratio of CO_3^{2-} to HCO_3^- in the starting $NaHCO_3$ solution. In 100 mM $NaHCO_3$ at pH 11 ± 0.2, the fraction of CO_3^{2-} increases to 50 – 72% with $\delta(^{13}C)$ located at 165.2 – 166.9 ppm. However, after mixing with 100 mM $CaCl_2$ solution, no signal between 162 and 172 ppm was detected by liquid-state ^{13}C NMR. Nevertheless, the initial concentration of the observed HCO_3^- signal was reduced to 10 – 20 mM (fig. S31-S32), suggesting that most $CaCO_3$ precipitates immediately upon formation and, thus, never exists in a liquid phase or does so for too short a time to be detected in our experiments. Due to the detection limit of ^{13}C NMR (about 1 mM under our experimental conditions), our quantitative analysis of HCO_3^- and CO_2 are not accurate at these dilute starting concentrations. However, we observed the same temporal trend for the smaller HCO_3^- signal as at low pH: broadening followed by resharpening, as well as continuous shifting to a lower frequency. Moreover, the initial shift of HCO_3^- to a higher frequency was more extreme at the higher initial pH: 1.0 ppm for pH 11.2 and 0.6 ppm for pH 10.8 vs. 0.3 ppm for pH 8.7. These changes may be explained by a very small amount of $Ca{\cdot}CO_3$ ion pairs trapped and released at the higher initial pH from a composite DLP containing both $Ca{\cdot}CO_3$ and $Ca{\cdot}HCO_3$. In other words, while the majority of $CaCO_3$ precipitates immediately from solution, a small amount of $Ca{\cdot}CO_3$ ion pairs associate with $Ca{\cdot}HCO_3$ ion pairs, which form a DLP, leading to broadening of the HCO_3^- signal. With further precipitation of this small amount of $CaCO_3$ at an initial pH of 11.2, or upon decomposition from $Ca(HCO_3)_2$ to form $CaCO_3$ at an initial pH 10.8 where the starting HCO_3^- is relatively higher, this composite DLP "dissolves" and most HCO_3^- becomes free, leading to sharpening of the HCO_3^- signal and eventually stabilized at 161.10 ppm. The ^1H T_2 of water experiences an initial increase instead of a drop at the higher pH, probably because a large amount of water molecules are released from hydrated ACC during the precipitation of the majority $CaCO_3$, which should significantly increase the water ^1H T_2.

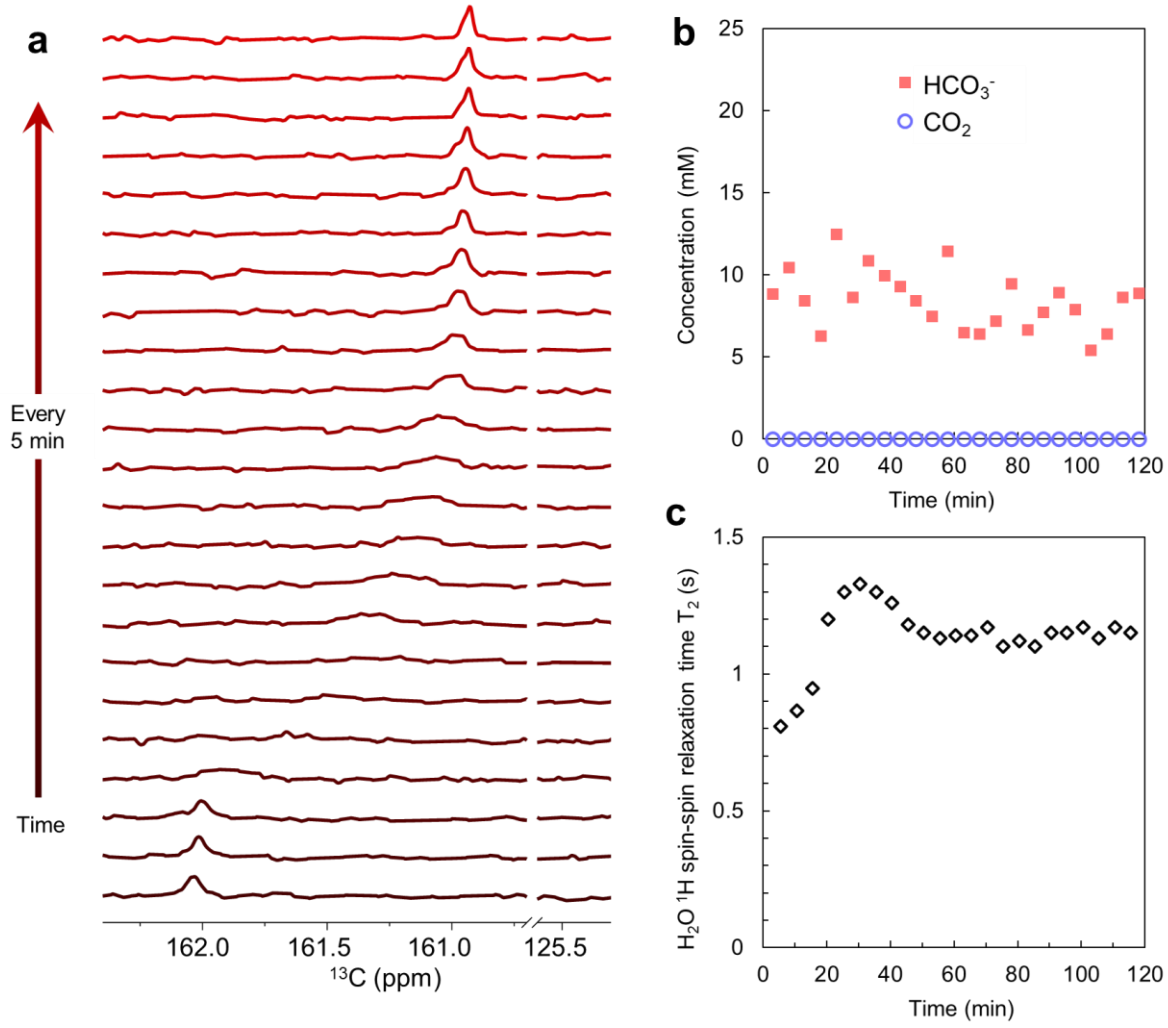

Figure S31. Time dependent ^{13}C NMR spectra (a) and the concentration evolution of HCO_3^- and CO_2 species (b) and H_2O ^1H spin-spin relaxation T_2 over time (c) after mixing 100 mM $NaHCO_3$ (pH 11.2) and 100 mM $CaCl_2$ (pH 6.9).

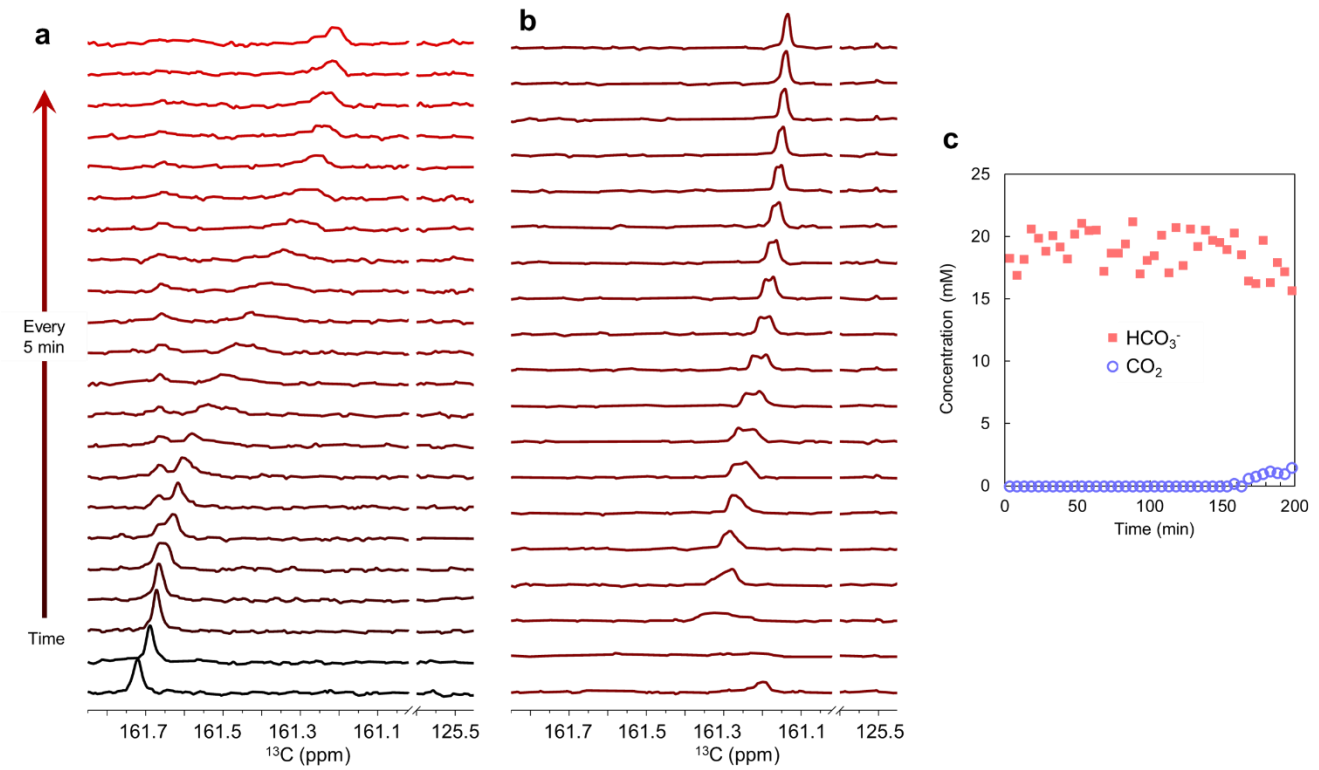

Figure S32. Time dependent ^{13}C NMR spectra (a, b) and the concentration evolution of HCO_3^- and CO_2 species (c) after mixing 100 mM $NaHCO_3$ with 0.8 μM DHR49Neg (pH 10.8) and 100 mM $CaCl_2$ (pH 6.9).

This composite DLP structure is similar to what's reported by Denis Gebauer, *et al*. recently[10]. They addressed the key role of HCO_3^- ions as active soluble species during the formation of ion pairs before nucleation. They stated that "At near-neutral pH, the existence of competition for interaction with calcium ions between carbonate and bicarbonate species produces distinct ion association behavior in the form of PNCs and ion pairs, respectively, the latter of which are negligible only above ca. pH 8.5–9.0." It is suggested that bicarbonate binds to terminal binding sites of calcium carbonate PNCs, and subsequently to the interfaces of the nascent nanodroplets through liquid-liquid phase separation. They thought DLP droplets consist of $CaCO_3$ PNCs with the existence of HCO_3^- at the interface. Later, bicarbonate ions become incorporated in the solid ACC upon dehydration of the liquid precursors. The existence of HCO_3^- in ACC was demonstrated by the solid-state NMR of dried ACC samples. These works show that the involvement of bicarbonate in calcium carbonate nucleation certainly cannot be excluded. However, they did not provide direct experimental evidence to show how HCO_3^- are involved into the amorphous phase or final crystalline phase. Therefore, using in situ liquid-state NMR and LP-TEM, we proposed that the pairing of HCO_3^- and Ca^{2+} occurs at the prenucleation stage, which act as soluble solute species for DLP formation.

Although we both study $CaCO_3$ formation from bicarbonate at near-neutral pH, our experimental conditions are different. In Gebauer's work[10], the solutions have much smaller starting and final concentrations. For example, the concentration of $CaCl_2$ is between 0.9 – 4.5 mM in their NMR samples, while we have 50 mM $CaCl_2$ in the mixed solutions. Another major difference is that they utilize slow titration of $CaCl_2$ into $NaHCO_3$ solution, while we perform rapid mixing of Ca^{2+} and HCO_3^- of high

concentrations at a molar ratio of 1:1. With the smaller concentration and much slower mixing at constant pH, each Ca^{2+} may have enough time to reach its lowest free energy (coordination to CO_3^{2-}) before another added Ca^{2+}, therefore $CaCO_3$ DLP may form with $Ca(HCO_3)_2$ terminating the surface (with a higher fraction of HCO_3 at a lower pH). In contrast, fast mixing of 100 mM Ca^{2+} (pH 6.9) and 100 mM HCO_3^- (pH 8.7) of equal volume allows the formation and growth of a metastable $Ca(HCO_3)_2$ DLP before $CaCO_3$ solidification even though $CaCO_3$ ion pair has lower Gibbs free energy than $CaHCO_3^+$ ion pair (-18.43 vs -7.42 kJ/mol)[10], primarily because water solvation of $Ca{\cdot}HCO_3$ ion associations lowers the free energy, as shown in our MD simulation and the previously reported DFT simulation of $Ca{\cdot}HCO_3$ clusters[19]. On the other hand, when we increase pH of 100 mM HCO_3^- to 11 ± 0.2, with the immediate drop in the concentration of HCO_3^-, we observe the similar composite DLP involving both CO_3^{2-} and HCO_3^-, but with HCO_3^- dominating over CO_3^{2-} under our experimental conditions. While liquid-state NMR cannot detect amorphous solids or crystals where molecular mobilities are much slower than in liquids or DLP, solid-state magic angle spinning (MAS) ^{13}C NMR spectra can directly monitor if these solid phases are involved over the course of the reaction.

The ^{13}C chemical shift drift with 0.8 μM DHR49-Neg and $NaHCO_3$ at pH 10.8 (fig. S32) seems significantly different from the control sample with $NaHCO_3$ at pH 11.2 (fig. S31), with an interesting drift back to high ppm then back to low ppm during 110 – 200 min. In order to double check that this drift back and forth is real or just some experimental fluctuation, we repeated the experiment with freshly prepared 100 mM $CaCl_2$ + 1.2 μM DHR49-neg solution and 100 mM $NaHCO_3$ (pH 10.85). Single-scan ^{13}C single-pulse NMR with a relaxation delay of 30 s and ^1H T_2 with an experimental time of 4.5 min were collected alternatively right after mixing the solutions. As shown in fig. S33a, ^{13}C spectra experience a similar pattern as in fig. S32 with the drift back to high ppm occurring at ~185 min and drift back to low ppm at ~200 min (the green region), suggesting that this drift is real despite being small and temporary. Moreover, the water ^1H T_2 shows more complexity than what was observed in the neutral pH solutions that may indicate a multi-stage process. We labeled the four local extrema shown in the curve of ^1H T_2 as Time 1 to 4 (fig. S33b) and marked these time points on the ^{13}C spectra. We also labeled time points a to c on some ^{13}C spectra to mark the beginning of some significant changes in the ^{13}C spectra.

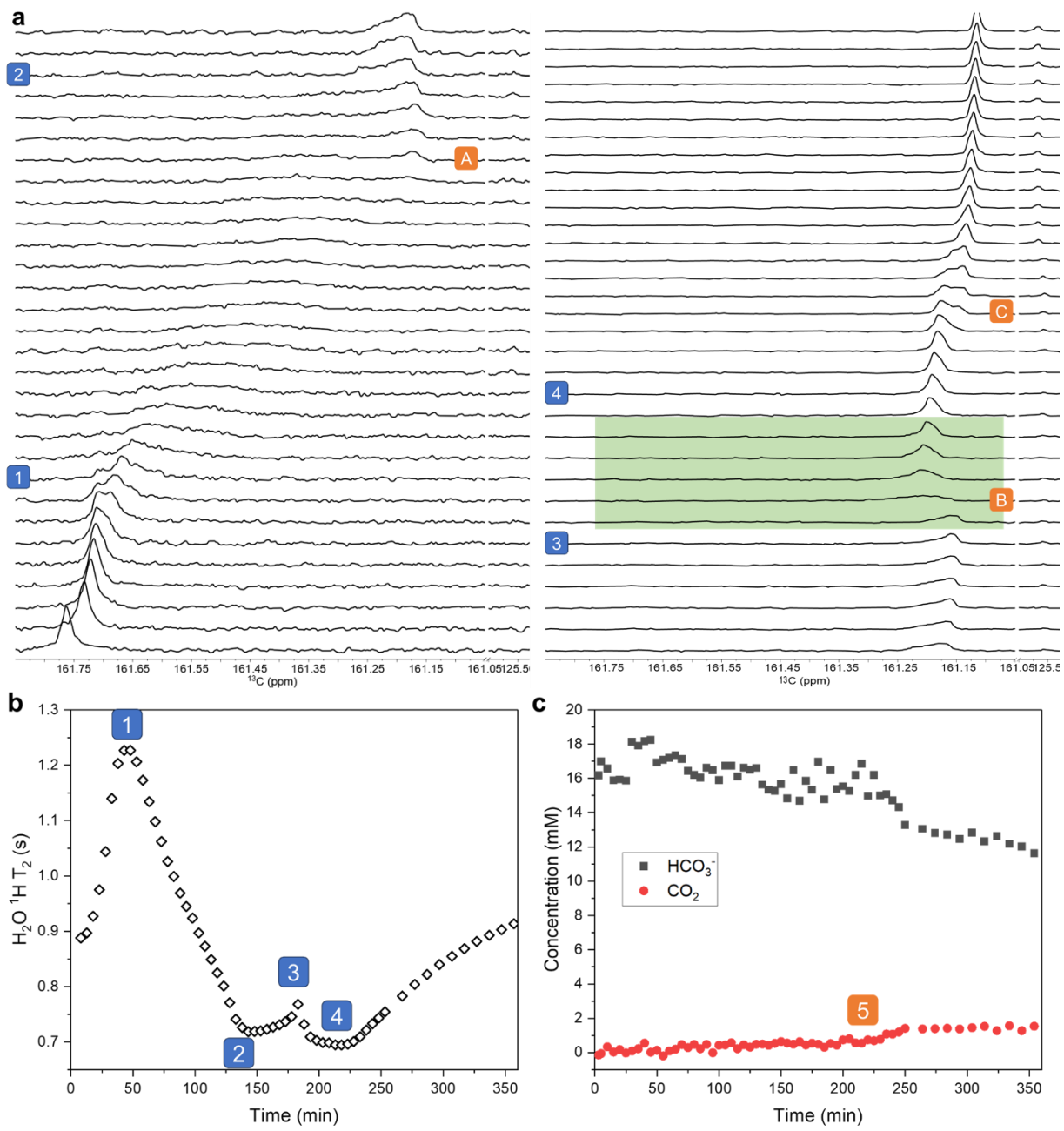

Figure S33. (a) ^{13}C spectra collected every 5 min after mixing freshly prepared 100 mM $CaCl_2$ + 1.2 µM DHR49-Neg solution and 100 mM $NaHCO_3$ (pH 10.85). (b) ^{1}H T_2 of water plotted as a function of time. (c) Concentration of "HCO_3^-" and CO_2 estimated from ^{13}C spectra.

The first reaction after mixing high pH $NaHCO_3$ and $CaCl_2$ is the instant formation of ACC, which is invisible from solution NMR. Estimated from what is left in the visible "HCO_3^-" signal, we can say that about 32 – 34 mM ACC was precipitated from the solution, which is close to the amount of CO_3^{2-} in the original $NaHCO_3$ pH 10.85 solution (33.4 mM) estimated from the ^{13}C chemical shift at 166.42 ppm. This precipitation releases water molecules that were previously coordinated to Ca^{2+} and CO_3^{2-} back to bulk solution, and therefore causes the initial increase in water ^{1}H T_2 (time 0 to 1).

The second reaction involves the formation of composite DLP consisting of both $Ca{\cdot}HCO_3$ and $Ca{\cdot}CO_3$ ion pairs. Consistent with what we have discussed previously, the single-line signal at 161.76 ppm is mainly $Ca{\cdot}HCO_3$ (aq) with a small amount of $Ca{\cdot}CO_3$ (aq). By using 161.4 ppm as the signal for neat $Ca{\cdot}HCO_3$ (aq) and 169.5 ppm (which is 169.2 + 0.3) as the signal for neat $Ca{\cdot}CO_3$ (aq), we can roughly estimate that the fraction of $Ca{\cdot}CO_3$ at 161.76 ppm is 4.4%. This signal shifts slightly to lower frequency, then becomes broad until time a (120 min); during this time, the water ^1H T_2 decreases due to the involvement of water in DLP formation (time point 1 to 2).
The decomposition of composite DLP with a relatively larger fraction of $Ca{\cdot}CO_3$ may comprise multiple stages. From time A, a ^{13}C signal between 161.15-161.25 grows from the very broad DLP signal. We assign this signal to the released "free" HCO_3^- due to the decomposition of a composite DLP. Because we do not detect a significant increase in CO_2, a logical assumption is that the first step of DLP decomposition is mainly the $Ca{\cdot}CO_3$ portion of the DLP transforming into ACC. This DLP decomposition also releases water and leads to an increase in water T_2 (time 2 to 3).
With the released "free" HCO_3^-, and with lack of CO_2, $Ca{\cdot}HCO_3^-$ starts to form ion pairs followed by a DLP of neat $Ca{\cdot}HCO_3^-$. This can explain the drift back to higher ppm at time B, and another decrease in water T_2 (time 3 to 4). This low-concentration $Ca{\cdot}HCO_3^-$- (DLP) again goes through formation (time B to C) and decomposition to produce ACC and CO_2 (time C –). This second decomposition finally leads to another increase in water T_2 (time 4 –). Here the time points where water dynamics change and where carbon speciation changes do not match exactly, because all we observed in ^{13}C and ^1H T_2 are the ensemble average; especially, ^1H T_2 is averaging out at about 3 min. Multi-stage DLP formation and decomposition may occur at different time scales for different droplets.

The overall summary of this pathway at higher pH is:
(1) instantaneous formation of ACC from $Ca{\cdot}CO_3$ ion pairing; (2) formation of a composite $Ca{\cdot}CO_3/Ca{\cdot}HCO_3$ DLP; (3) DLP decomposition by transforming most of the $Ca{\cdot}CO_3$ in the DLP into ACC and releasing HCO_3^- to bulk solution; (4) renewed ion pairing and of formation of new $Ca{\cdot}HCO_3$DLP do to the HCO_3^- release; and (5) $Ca{\cdot}HCO_3$ (DLP) decomposition to form $CaCO_3$, CO_2 and water.

Through comparison to the reaction without DHR49-Neg (fig. S31), we can see that the major role of the protein is to stabilize both the composite DLP and $Ca{\cdot}HCO_3$ (DLP), and to slow down the decomposition of both DLPs.

Effect of LP-TEM, solution- and solid-state NMR experimental configurations on observations of nucleation processes

With liquid-cell TEM and solution- and solid-state NMR being increasingly utilized for in-situ monitoring of nucleation processes, this section will discuss how the different experimental configurations of TEM and NMR can affect the observed nucleation rates and pathways. Due to the delicate nature of nucleation processes, particularly those involving the formation and transformation of dense liquid droplets, precipitation of amorphous solids, and generation of gas, we will consider six factors related to experimental setups that may impact the nucleation process.

Sample dimensions. With the schematic drawings shown in fig. S34, the first obvious difference in the experiments is the size of the reacting solution used in the measurements. The sample cell for liquid-cell TEM in a spacer chip has a dimension of 3 mm × 3 mm × 100 nm (total volume 0.9 µL), with an imaging area of ~50 µm × 50 µm. On the other hand, a 5 mm NMR tube for solution-state NMR in has an inner diameter of 4.0 mm and a length of about 180 mm (total volume 2260 µL). The sample solution usually fills a length of 40 mm, with the middle 20 mm being excited and detected by radiofrequency (RF) coils. Similarly, a 5 mm sealable WHiMS NMR rotor for solid-state NMR (ssNMR) has an ID of 3.37 mm and a length of 15 mm (total volume 133 µL), with the entire length wrapped by RF coils for excitation and detection.

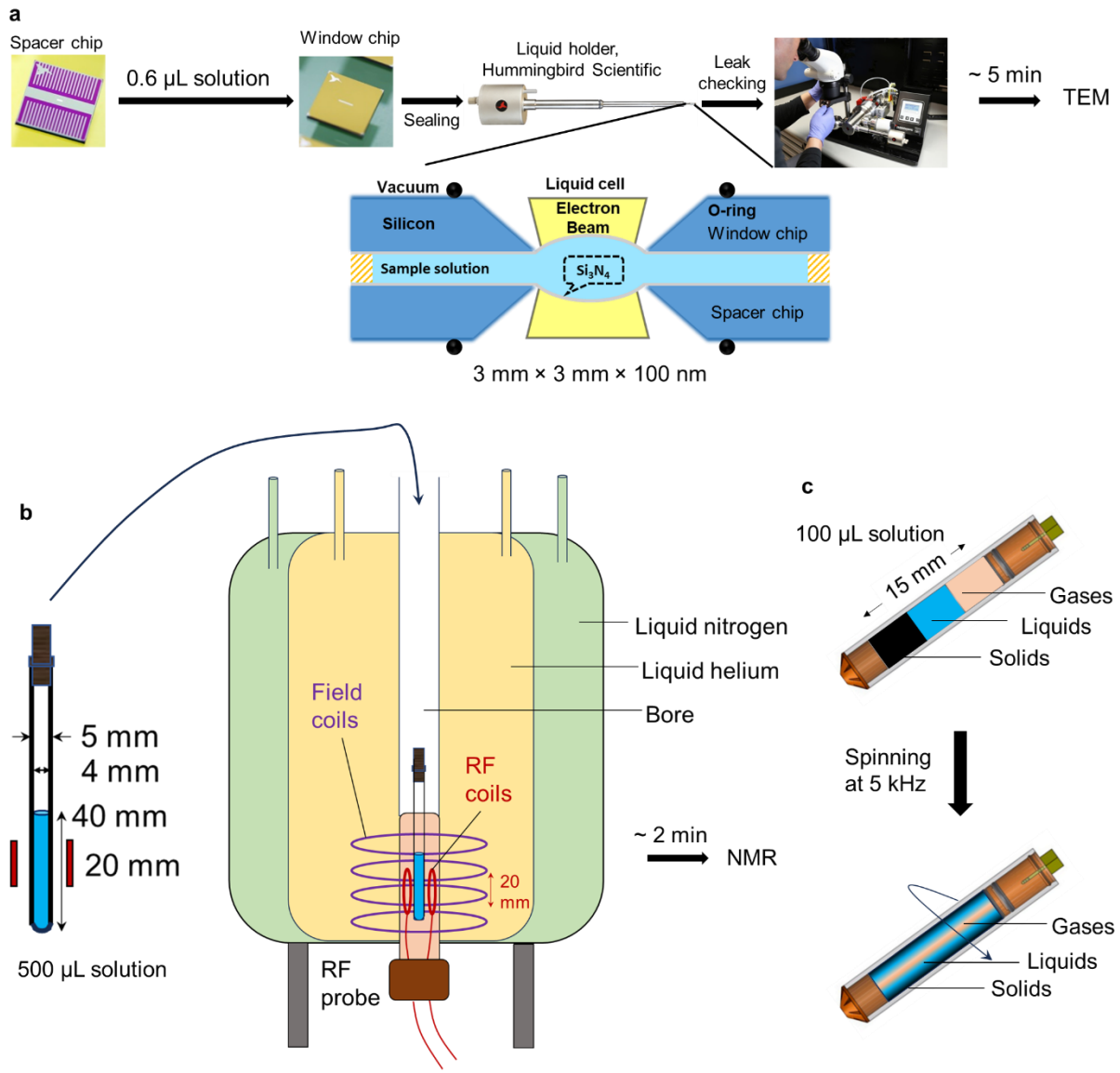

Figure S34. Different experimental configurations for liquid-cell TEM (a), solution-state NMR (b) and (c) solid-state NMR.

In a classical nucleation process, the possibility $P(t)$ of forming at least one nucleus in a time interval t is directly related to the sample volume V, $P(t) = 1 - \exp(-JVt)$, here J is the stationary nucleation rate.[20] Although the nucleation from Ca^{2+} and HCO_3^- in solutions to $CaCO_3$ follows a non-classical pathway, the possibility of forming ion pairs and the sequent transition to DLP and ACC could be also highly related to the sample volume. Therefore, the remarkable difference in the sample volume (0.6 µL in LP-TEM vs. 500 µL in solution NMR vs. 100 µL in ssNMR) will lead to differences in the observed induction times and nucleation rates during the measurements.

Surface vs. bulk. Related to sample dimensions, the surface to volume ratio of the thin layer of sample solution in a LP-TEM cell (2×10^4 mm^{-1}) is much larger than that of the sample solution in an NMR tube (1 mm^{-1}) or an NMR rotor (1.2 mm^{-1}). While Si_3N_4 ceramics is considered thermodynamically stable and chemically inert, the reaction solution closely contacting to Si_3N_4 surface at a large surface to volume ratio may still likely affect the delicate nucleation process.

Electron beam vs. RF radiation. With the minimum electron dose rate utilized during imaging process to minimize the electron beam damage in LP-TEM, we have demonstrated that radiolysis is not the reason for the observation of DLP and ruled out any effect of heating caused by the electron beam. However, compared to the truly non-invasive non-ionizing RF radiation employed in NMR, the electron beam may still affect the rates at which DLP forms and transforms through its interaction with solvent molecules or solute ions, or by reducing the solution pH.

Airtightness. Liquid cells in LP-TEM are hermetically sealed to enclose the solution from the high vacuum environment within the TEM, the airtightness is crucial for the imaging. In contrast, for solution NMR, a plastic cap is typically used, which is not sealed, therefore any gas dissolved in the solution or generated during the reaction may leak out of the detection region once the solubility is reached; for the WHiMS rotors used in our ssNMR measurements, the seal is airtight under static condition, however, gas may leak out of the rotor slowly with time as the fast spinning of the rotor employed during MAS experiments may disturb the seal over time.

Mechanical and thermal perturbations. Mechanical and thermal perturbations are completely absent from solution NMR, because the NMR tube is maintained inside the core of the magnet at a pre-set temperature steadily over the course of the measurements. The movement of the electron beam when switching imaging spots may introduce some artificial displacement, especially considering the depth of only 100 nm in the sample cell. SSNMR encounters the most mechanical and thermal perturbations due to the fast spinning of the rotor (5 kHz used in this work). The fast spinning of a sample experiencing mixed phase reactions may introduce the following disadvantages: 1) the spinning mix the solutions much more vigorously than in the static state, 2) the shearing stress from the spinning may act differently on the solids, liquids and gases and thereby change reaction rates, 3) the great centrifugal force from the spinning may further separate these phases into different layers and alter reaction pathways, 4) the heat generated from the spinning acts differently at different layers; the outer layer closet to the rotor wall may experience an increase of 1 – 20 K from the pre-set temperature depending on the spinning speed and rotor size. But in some cases, the spinning may just change the reaction rate and allows for the detection of the amorphous or crystalline phases that are invisible in solution NMR.

Delay between solution mixing and measurement. Once the two solutions are mixed and placed in the spacer chip, TEM measurements can start after less than 5 min of instrument preparation. This delay is around 1 – 2 min in solution NMR and 3 min in ssNMR. Therefore, the initial few minutes of change in the reacting solution will not be accessible using LP-TEM or NMR. Microfluidic probes where the individual solutions can be delivered to the sample cell and the mixing occurs right before the measurements can minimize the delay. While these microfluidic probes can be implemented in both TEM and NMR, they were not used in this work, because 1) the delays are manageable due to the induction time of nucleation; 2) microfluidic flow may introduce other perturbations in nucleation.

Considering these differences in experimental configuration, we can begin to understand the distinct characteristics of DLP droplets observed using LP-TEM and solution NMR. In the liquid cell of LP-TEM, several factors such as the confinement (a hermetically sealed solution with a thickness of 100 nm), membrane interactions (due to a high surface to volume ratio in close contact with Si_3N_4), and minor electron beam effects (radiolysis products, reduced solution pH, and displacement) collectively contribute to the observed gel-like DLP with an estimated viscosity of ~10^6 Pa·s. While these effects do not directly cause DLP formation, confinement and membrane interactions likely reduce molecular mobilities within DLP, and minor beam effects may lead to the formation of larger DLP volumes, resulting in a DLP with more gel-like features. In contrast, the controlled steady environment of solution NMR, with a small surface to volume ratio and in the absence of any mechanical, thermal, or ionization perturbations, reflects

undisturbed DLP behavior in bulk solution. DLP observed under these conditions are highly dynamic, and much more liquid-like compared to DLP observed in LP-TEM.

In addition, the generation of CO_2 during DLP decomposition may influence DLP transformation differently under the varying sealing conditions in TEM and NMR. However, as this study primarily focuses on DLP formation and transformation prior to a significant CO_2 generation, the potential effects of CO_2 in different experiments can be minimized in our discussions.

Given the significant mechanical and thermal perturbations caused by the spinning of NMR rotors in ssNMR and the delicate nature of DLP, we have limited insight into how the DLP formation and transformation pathways may be affected under these conditions. Therefore, we do not intend to utilize ssNMR to capture these pathways. Instead, our focus is solely on using ssNMR to detect the formation of $CaCO_3$ ACC, which is not observable via solution NMR. We then analyze the stoichiometric changes of bicarbonate in solution, CO_2 in gas phase, and $CaCO_3$ ACC or calcite in solid phase by comparing the experiments conducted at pH 8.7 and pH 10.8.

Differences in structure of calcium (bi)carbonate solutions between DFT-based and empirical potentials

The literature regarding the use of condensed DFT for predicting the structure of calcium (bi)carbonate solutions remains unsettled[23]. A qualitative difference in the Ca---$C_{carbonate}$ PMF between our study[22] and that of Raitieri et al.[24] is reported. The origin of this discrepancy involves differences in the coordination state of the "free" calcium ion[25] not simulation protocols as has been suggested[24]. Using similar simulation protocols to those of the present study and of Henzler et al.[23], Baer and Mundy[25] provided a detailed study of the Ca^{2+} solvation structure, finding that the most likely coordination state of Ca—O is ~7 with populations of 6-fold coordinated being on the ~1 kcal/mol higher in free energy. The work in Raitieri et al.[24] was performed for different ensembles and systems sizes, including a slab geometry where density effects can be considered. In that study, the two coordination states of Ca^{2+} do not agree quantitatively with those obtained in Henzler et al.[23]. Importantly, the 6-fold coordinated state of Ca—O is found to be more stable by ~1 kcal/mol (see Fig. 4 of Raitieri et al.[24]). We speculate that these discrepancies will likely lead to different 1-dimension PMFs of ion-binding (Ca---$C_{carbonate}$) as the pathways between coordination states will be different. The coordination states for this study are reported in Henzler et al.[16] where we find predominantly ~7-fold Ca—O coordination for Ca—C distances > 4 Å.

The calculation of water content and DLP density

Based on our *in situ* NMR results, the DLP consists of a highly hydrated $Ca(HCO_3)_2{\cdot}nH_2O$ droplet. H_2O plays an important role in the DLP formation as a key component, and thus it is necessary to calculate water content in DLP. During the transformation process of DLP into hydrated ACC solids ($CaCO_3{\cdot}H_2O$), a pathway could be described by the following reaction:

$$Ca(HCO_3)_2{\cdot}nH_2O(DLP) \longrightarrow CaCO_3{\cdot}H_2O_{(hydrated\ ACC\ solid)} + CO_2 + nH_2O$$

During this reaction, the release of CO_2 and H_2O can reduce the mass and volume of the initial DLP. As reported before, the volume change of DLP arises from the removal of H_2O. LP-TEM technique is an effective approach to in situ follow the size change of individual particles. To determine the water content, we quantitatively analyzed the dehydration process of DLP through in situ measurement of the change in radius of DLP droplets. Assuming the comparable volume between DLP droplets and hollow particles (fig. S35 and Fig. 3a), we followed the volume evolution of 15 hollow particles to hydrated ACC solids. The following equations (1-2) and the parameters in table S4 are used to estimate the water content, revealing the n is 7.5±1.7. Furthermore, from the averaged n value, the DLP density is determined to be about 1.36 g/cm^3 based on equations (3-4)[6].

$$\frac{\rho_{ACC}V_{ACC}}{\rho_{H2O}V_{H2O}} = \frac{m_{ACC}}{m_{H2O}} = \frac{118}{18n} \qquad (1)$$

$$n = \frac{118\rho_{H2O}V_{H2O}}{18\rho_{ACC}V_{ACC}} = 4.3\frac{V_{H2O}}{V_{ACC}} \qquad (2)$$
$$= 4.3\left(\frac{V_{DLP}}{V_{ACC}} - 1\right)$$
$$= 4.3\left(\frac{r_1^3}{r_2^3} - 1\right)$$

$$\frac{\rho_{DLP}}{\rho_{ACC}} = \frac{m_{DLP}V_{ACC}}{m_{ACC}V_{DLP}} = \frac{m_{DLP}r_2^3}{m_{ACC}r_1^3} \qquad (3)$$

$$\rho_{DLP} = \rho_{ACC}\frac{m_{DLP}r_2^3}{m_{ACC}r_1^3} \qquad (4)$$

Based on the chemical reaction of DLP to ACC as described above, we can also propose the below equations (5-8) for estimating the water content (n) as a comparison:

$$\frac{m_{DLP}}{m_{ACC}} = \frac{\frac{\rho_{DLP}}{\rho_{Bkgrd}}V_{DLP}}{\frac{\rho_{ACC}}{\rho_{Bkgrd}}V_{shell}} = 1 + \frac{m_{CO2+H2O}}{m_{ACC}}$$

$$= 1 + \frac{\left({}^{m_{ACC}}/_{M_{ACC}}\right)\bullet(M_{CO_2}+nM_{H_2O})}{\rho_{ACC}V_{shell}}$$

$$= 1 + \frac{\left({}^{\rho_{ACC}V_{shell}}/_{M_{ACC}}\right)\bullet(M_{CO_2}+nM_{H_2O})}{\rho_{ACC}V_{shell}}$$

$$= 1 + \frac{(M_{CO_2}+nM_{H_2O})}{M_{ACC}} \qquad (5)$$

$$\frac{\frac{\rho_{DLP}}{\rho_{Bkgrd}}V_{DLP}}{\frac{\rho_{ACC}}{\rho_{Bkgrd}}V_{shell}} = 1 + \frac{(M_{CO_2}+nM_{H_2O})}{M_{ACC}} \qquad (6)$$

$$n = \frac{M_{ACC}}{M_{H2O}}\left[\frac{\left(\frac{\rho_{DLP}}{\rho_{Bkgrd}}\right)}{\left(\frac{\rho_{ACC}}{\rho_{Bkgrd}}\right)}\frac{V_{DLP}}{V_{shell}} - 1\right] - \frac{M_{CO_2}}{M_{H_2O}} \qquad (7)$$

And then plugging the ratios of the molecular weights $M_{ACC} = 118$, $M_{H2O} = 18$, $M_{CO2} = 44$, we can get:

$$n = 6.6\left[\frac{\left(\frac{\rho_{DLP}}{\rho_{Bkgrd}}\right)}{\left(\frac{\rho_{ACC}}{\rho_{Bkgrd}}\right)}\frac{V_{DLP}}{V_{shell}} - 1\right] - 2.4 \qquad (8)$$

We calculated an upper limit of n based on a relative density of 1.0 due to the similarity of the gray scale values in the shell and at the rim of the droplet as seen in Fig. 3b, and another value based on above estimate of DLP density (1.36 g/cm^3), which gives a relative density of 0.91. We also notice that the average value of the relative volume of the DLP droplet to the resulting ACC is 2.7 (fig. S35b), that is the upper limit of (V_{DLP}/V_{shell}). Based on the proposed relative densities of DLP to ACC of between 0.9 and 1.0 and the V_{DLP}/V_{shell} of 2.7, we can estimate a range of n values between 7.0 and 8.8, consistent with the

above calculation method. A representative example is showed in fig. S36c, where V_{DLP}/V_{shell} is 2.4, giving a range of n values 6.8. Also note, however, that the size of the shell has some uncertainty as it is difficult to know at which moment it should be measured, since is thickens with time. In the calculation, we have calculated the value at the time it first forms, prior to its thickening into ACC.

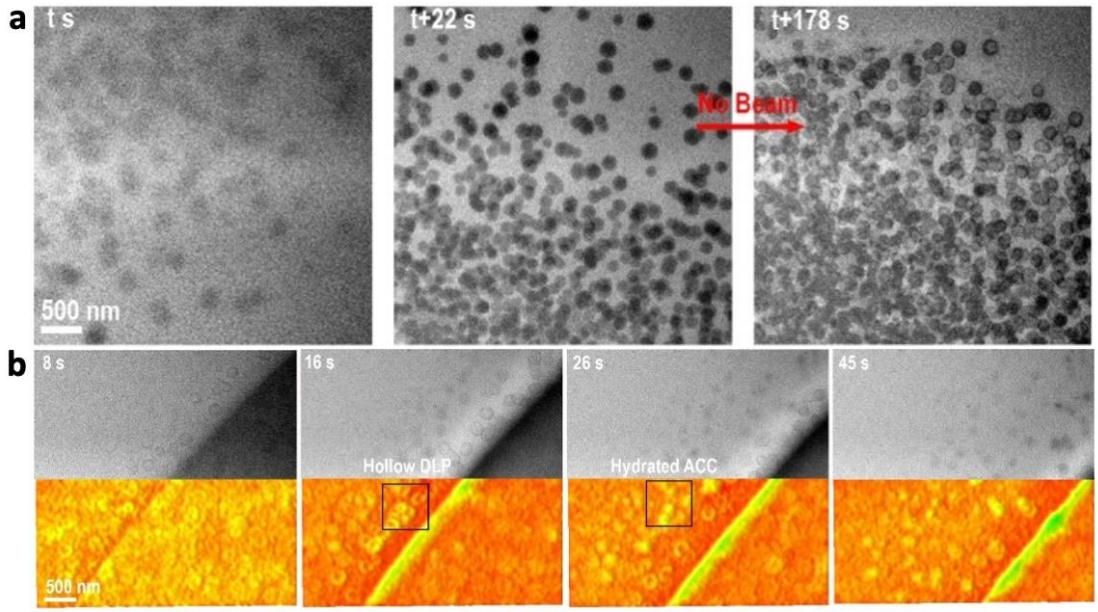

Figure S35. LP-TEM images show widespread evolution of DLP droplets formed in the presence of DHR49-Neg proteins into hollow particles (a) when the electron beam is blocked at all times except while searching the area of interest, adjusting the focus, and acquiring images, and (b) during gradual dehydration of hollow particles as liquid/gas meniscus moved across the liquid cell.

The estimation of shell volume percentage

We measured the radius (R) of the hollow particles and the thickness (T) of the shell (fig. S36), and then calculated that the volume of the shell relative to that of the particle is given by $1-r^3/R^3$, where r = R-T. By calculating 13 hollow particles, we estimated the averaged value is 76% (table S3). The results show that the shell constitutes about 76% of the particles volume, which indicates that a thin shell has a relatively large volume.

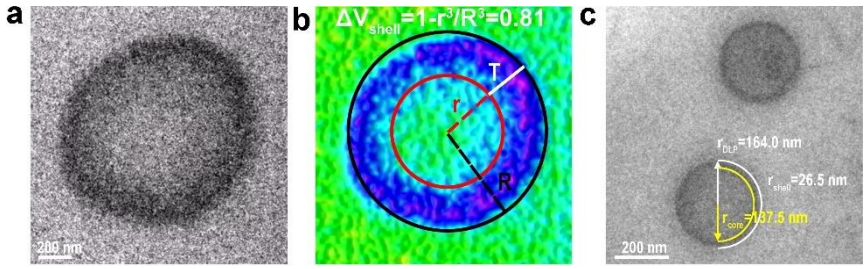

Figure S36. The estimation of shell volume percentage and the estimation of water content. (a) A representative TEM image showing an individual hollow particle. The hollow structure was formed in the presence of DHR49-Neg proteins. (b) Schematic illustration for the calculations of shell volume percentage. (c) The measurements illustration of DLP radius and shell thickness, revealing the relative volume of DLP to shell of 2.4.

Table S3. The estimated shell volume percentages relative to the particles

	1	2	3	4	5	6	7	8	9	10	11	12	13	Average
V_{shell} (%)	76	78	80	72	78	77	76	79	72	72	76	74	81	76

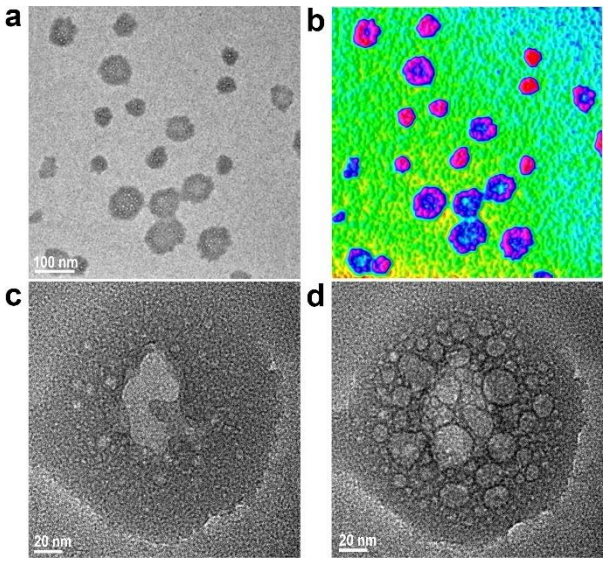

Figure S37. Ex situ TEM (a) and false-colored images (b) show the hollow ACC solids in the presence of DHR49-Neg proteins. (c-d) TEM images of two single ACC particles with higher resolution, clearly showing the existence of voids in the centre of particle.

Table S4. The parameters for the calculation of water content and DLP density

	$Ca(HCO_3)_2 \cdot nH_2O$(DLP)	$CaCO_3 \cdot H_2O$(hydrated ACC solid)	H_2O
Density (g/cm^3)	ρ_{DLP}	$\rho_{ACC}=1.49$	$\rho_{H2O}=1.0$
Volume	$V_{DLP}=4\pi/3r_1^3$	$V_{ACC}=4\pi/3r_2^3$	$V_{H2O}= V_{DLP}- V_{ACC}$
Mass	$m_{DLP}=162+18n$	$m_{ACC}=118$	$m_{H2O}=18n$

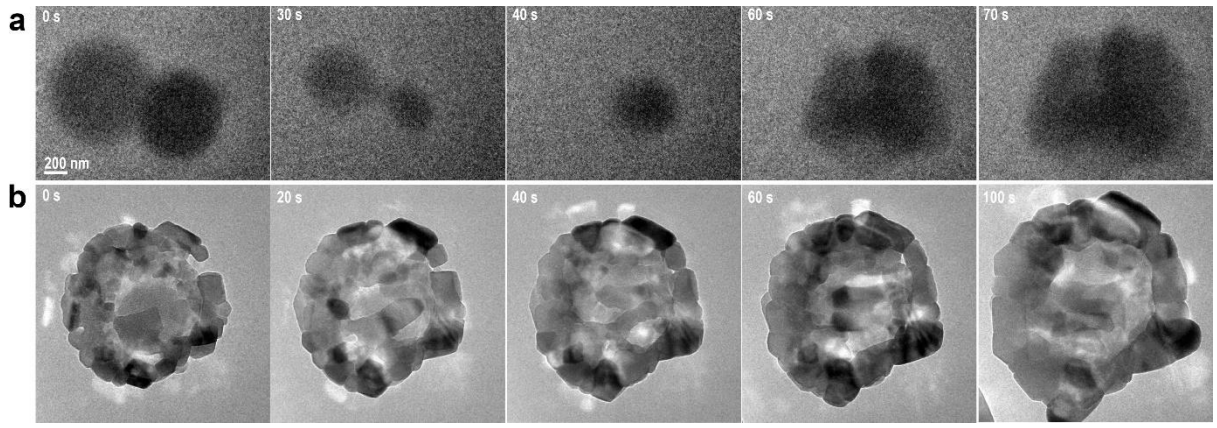

Figure S38. Time dependent TEM images show the amorphous phase mediated crystallization process in the presence of DHR49-Neg proteins. (a) The dissolution of amorphous particles, followed by the recrystallization into calcite in solution. (b) The dissolution of amorphous particles, leading to the growth of crystals at the interface of amorphous and crystalline particles.

Molecular simulations of DLP structure and stability

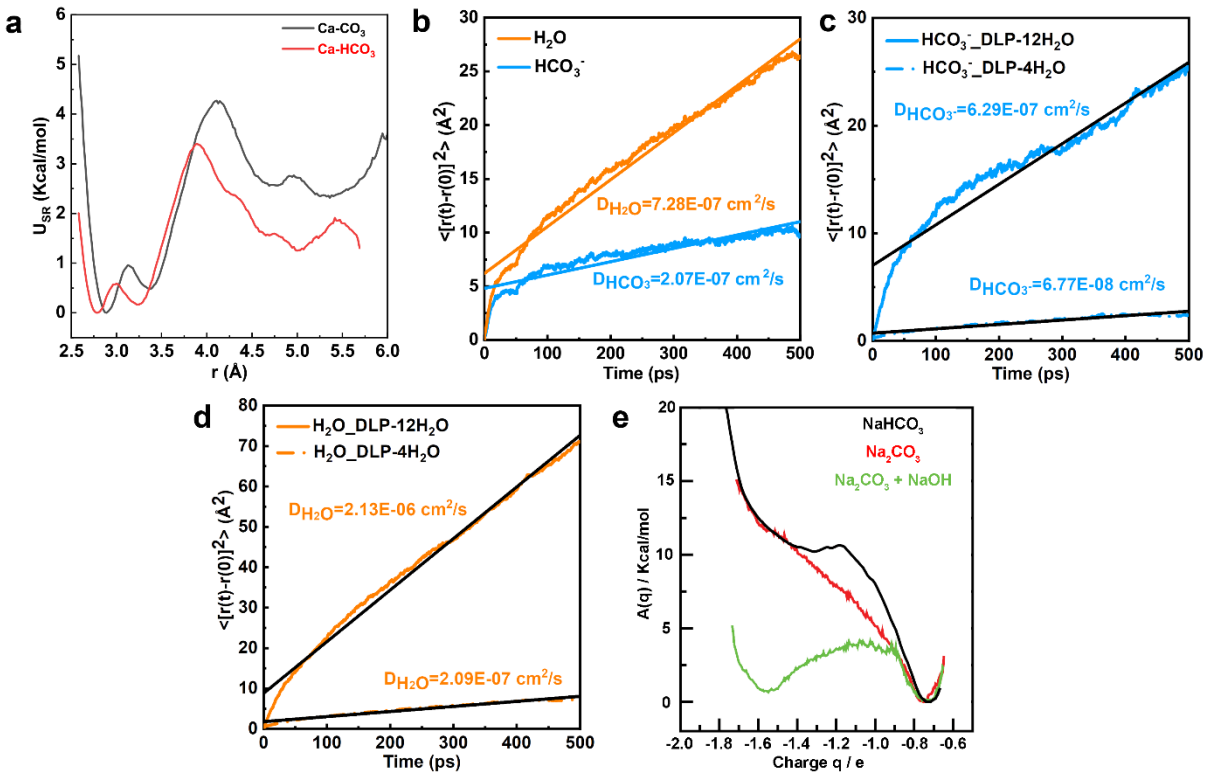

Figure S39. Simulations for DLP structure and diffusion constants extraction. (a) The computed the SR PMF between Ca--HCO_3 and Ca--CO_3. Beyond 6 Å we utilize a Coulombic term that is represented by 1^epsilon r, where epsilon is 80 and used to represent he dielectric constant of bulk water. (b) Mean square deviation of solution species as a function of time in molecular dynamics simulation of bulk DLP models ($(CaHCO_3)_2 \cdot 7H_2O$)). The calculated diffusion coefficient of H_2O is smaller than that of HCO_3^-. The offsets denote local/rotational/vibrational degrees of freedom which are substantially larger for water than for bicarbonate. (c-d) Mean square deviation of solution species as a function of time in molecular dynamics simulation of bulk DLP models with different hydration levels raging from 4 to 12 H_2O per ion pair. (e) AIMD calculations during numerical titration experiments. CO_3^{2-} free energy as a function of net charge state, A(q), determined by sampling AIMD simulations of an ion in bulk water at three notional pH values. The global minimum in the A(q) curves represents predicted stable charge states. Certain intermediate titration experiments show multiple local minima, thus predicting mixed populations of accessible charge states.

In the spirit of our previous study[23], we modeled Ca^{2+} and HCO_3^- as a charged sphere interacting in an intervening dielectric medium. Instead of utilizing Monte Carlo moves to sample the aggregation states,[24] we note the similarity between the free energy landscapes for the pairing of Ca^{2+} with either HCO_3^- or CO_3^{2-} and rely on a combination of a frustrated-charge Ising model (FCI) in conjunction with all-atom molecular dynamics (MD) to model this condensate as a DLP. We utilized the FCI model on a lattice where the short-range "Ising" interaction is replaced with a discretized PMF obtained from previous work[16] between HCO_3^- or CO_3^{2-} (and all other unique pairs) in conjunction with long-range Coulomb interactions modified by the static dielectric constant of pure liquid water (fig. S40). The concentration of the ions comprising the lattice simulations is chosen to be consistent with the measured water content of

the DLP (table S4). The resulting simulations provide the sampling of the ion—ion correlations and describe a charge-neutral HCO_3^- and Ca^{2+} solution represented by charged spheres where all the short-range molecular detail is encoded in the PMF (fig. S40). From the results of the FCI simulation, we reconstitute the molecular detail by re-introducing the all-atom representation using the classical force field[26], which defines our molecular model for the observed DLP.

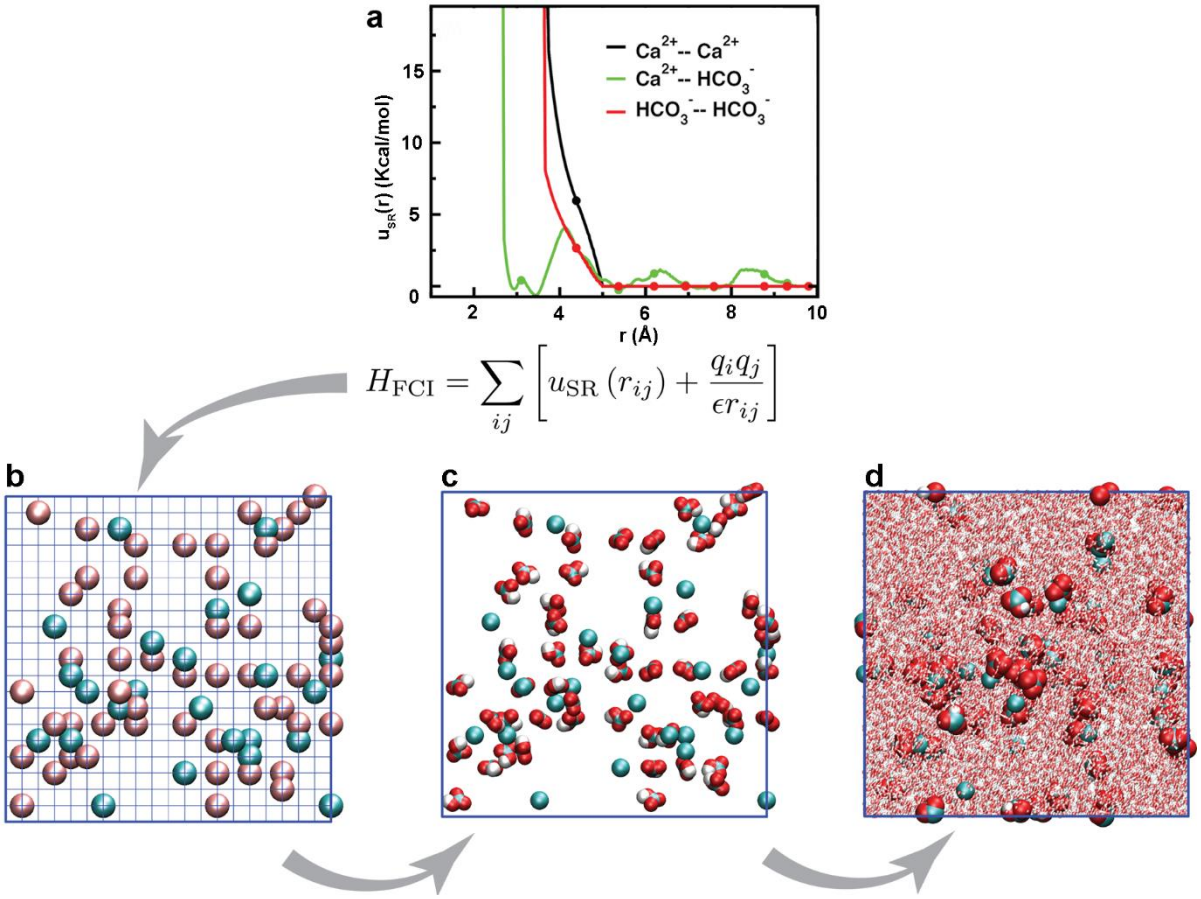

Figure S40. A schematic for the workflow for our reduced model for DLP structure. (a) The potential of mean-force (PMF) between ions as done in Henzler et al. with the Coulomb term subtracted out. The PMF is sampled at lattice points (a=3.1Å) as shown by the points. This is used as input for u_{SR} the frustrated charge Ising model (FCI). The long-range contribution is the Coulomb interaction modulated by the dielectric constant. (b) The FCI is used to generate ensembles of charges interacting on a lattice with the mean-field water (through the PMF) at the experimental number density. Ca^{2+} is depicted by cyan sphere, HCO_3^- (and/or CO_3^{2-}) is denoted by red sphere. (c) Ensembles are then with molecules with random orientations (here HCO_3^- and Ca^{2+}). (d) Water is added and the simulations are converged with standard all-atom force fields.

Further discussion of implications

The fact that the DLP is formed at low pH (~ 8 to 10) from HCO_3^- and releases CO_2 upon transformation to $CaCO_3$ but is either absent or transient at high pH (> 11), implies that, if DLP indeed plays a role in biomineral formation, pH regulation is an important function in mineralizing systems. Although the interfacial pH in a biological system remains unknown, the successful detection of HCO_3^- ions on the amorphous mineral/organic interface in stony corals[27] implies a lower pH at the growth front, which suggests that organisms may indeed be able to manipulate bicarbonate levels via local pH to sustain calcification via a DLP. Moreover, in abiotic reservoirs of metal carbonate formation, the effect of pH on mineralization rates, macrostructures and impurity and isotopic signatures, must now be extended to include the extent to which the pH is conducive to the formation of the DLP. Thus, a hopeful extension of our work would be to investigate how HCO_3^- in the environment impacts mineral polymorph selection and regulates the morphology of final crystalline phases. On the other hand, given that one can design synthetic proteins to modulate the rates of formation and transformation of the DLP at a given pH, utilization of this strategy following CO_2 capture suggests an approach to producing moldable forms of carbonate cements.

The NMR results (Fig. 2) also show that, like DLP formed in additive-free solutions, PILP and protein-stabilized DLP are composed of $Ca^{2+} + 2HCO_3^-$ plus water and undergo the same chemical transformation but do so on longer time scales. However, it remains to be determined whether the polymers and proteins are incorporated into the DLP or are adsorbed onto DLP droplets and how they alter the DLP stability and transformation rates. The longer DLP lifetime is likely due to the higher charge-to-surface ratio associated with the COO^- groups, which strongly interact with Ca^{2+} as indicated by ^{43}Ca NMR spectra (fig. S10)[28]. Our hypothesis is that these COO^- groups provide a sink for Ca^{2+} that competes with HCO_3^- to promote stabilization of the DLP[23,28]. Regardless of the mechanism, the effect on the time scale for formation and transformation still has important implications for mineralization, whether in biological, geochemical or technological settings, due to the dimensions to which DLP can grow before transformation and the effect on rates of mass and energy transfer that determine key features like morphology and style of transformation, such as pseudomorphic or dissolution-reprecipitation.

The combination of the laboratory results and observations from natural systems provides further circumstantial evidence that the DLP serves as a precursor to crystalline $CaCO_3$ biominerals. Laboratory results show that the highly charged protein DHR49-Neg and negatively charged PAA both significantly extend the timescale for DLP formation and transformation and that highly positively charged Poly (allylamine hydrochloride) also produces PILP[29]. Observations from natural systems show that highly charged proteins, both negative[30] and positive,[31] are common components of biominerals exhibiting hierarchical structure, complex morphology, and liquid-like features[30]. Moreover, the ability of the PILP process to create mineralized collagen that closely resembles that of trabecular bone[32,33], as well as reports of hollow calcium phosphate particles[34], suggests a DLP consisting of condensed Ca^{2+} and $H_2PO_4^-$ ions with their solvation shells may well exist in the calcium phosphate system and likewise evolve to amorphous calcium phosphate and subsequent crystalline phases through a process similar to that reported here. The well-documented involvement of the aspartic-acid rich protein osteopontin (OPN) in bone deposition[35] further suggests that, if a calcium phosphate DLP exists, it is stabilized by OPN, as proposed by Gower and co-workers[36] and Nudelman et al.[37] Moreover, the observation of outward to inward solidification of DLP droplets into hollow ACC particles at the nanoscale establishes a connection to previously reported hollow helices formed from a DLP at the microscale[38] and the disinclination lines seen in the densification of PILP droplets at the macroscale.[39]

References

1. Brunette, T. *et al.* Exploring the repeat protein universe through computational protein design. *Nature* **528**, 580-584 (2015).
2. R. Mashiach et al. In situ NMR reveals real-time nanocrystal growth evolution via monomer-attachment or particle-coalescence. *Nat. Commun.* **12**, 229 (2021).
3. Assighaou, S. & Benyahia, L. Universal retraction process of a droplet shape after a large strain jump. *Phys. Rev. E* **77**, 036305, (2008).
4. Koishi, A., et al. Surface wetting controls calcium carbonate crystallization kinetics. *Chem. Mater.* **31**, 3340, (2019).
5. Wolf, S. L., et al. Gel-like calcium carbonate precursors observed by in situ AFM. *Langmuir*, **33**, 158, (2017).
6. Rao, A., Huang, Y.-C. & Cölfen, H. Additive speciation and phase behavior modulating mineralization. *J. Phys. Chem. C* **121**, 21641-21649, (2017).
7. Nebel, H., Neumann, M., Mayer, C. & Epple, M. On the structure of amorphous calcium carbonate: A detailed study by solid-state NMR spectroscopy. *Inorg. Chem.* **47**, 7874-7879 (2008).
8. Högfeldt, E. & Bigeleisen, J. Acidity constants of some hammett indicators in heavy water. The hammett acidity function, D0, for DCl and D_2SO_4 Solutions. *J. Am. Chem. Soc.* **82**, 15-20 (1960).
9. Abbott, T. M., Buchanan, G. W., Kruus, P. & Lee, K. C. ^{13}C nuclear magnetic resonance and Raman investigations of aqueous carbon dioxide systems. *Canad. J. Chem.* **60**, 1000-1006 (1982).
10. Huang, Y. C. *et al.* Uncovering the role of bicarbonate in calcium carbonate formation at near-neutral pH. *Angew. Chem. Int. Ed.* **60**, 16707-16713, (2021).
11. Zhao, D. F. *et al.* Novel method of generation of $Ca(HCO_3)_2$ and $CaCO_3$ aerosols and first determination of hygroscopic and cloud condensation nuclei activation properties. *Atm. Chem. Phys.* **10**, 8601-8616, (2010).
12. Wolf, S. E. *et al.* Strong stabilization of amorphous calcium carbonate emulsion by ovalbumin: gaining insight into the mechanism of 'polymer-induced liquid precursor' processes. *J. Am. Chem. Soc.* **133**, 12642-12649, (2011).
13. Ramnarain, V. *et al.* Monitoring of $CaCO_3$ nanoscale structuration through real-time liquid phase transmission electron microscopy and hyperpolarized NMR. *J. Am. Chem. Soc.* **144**, 15236-15251 (2022).
14. Soli, A. L. & Byrne, R. H. CO_2 system hydration and dehydration kinetics and the equilibrium CO_2/H_2CO_3 ratio in aqueous NaCl solution. *Mar. Chem.* **78**, 65-73 (2002).
15. Abbott, T. M., Buchanan, G. W., Kruus, P. & Lee, K. C. ^{13}C nuclear magnetic resonance and Raman investigations of aqueous carbon dioxide systems. *Can. J. Chem.* **60**, 1000-1006 (1982).
16. Camper, D., Bara, J., Koval, C. & Noble, R. Bulk-fluid solubility and membrane feasibility of rmim-based room-temperature ionic liquids. *Ind. Eng. Chem. Res.* **45**, 6279-6283 (2006).
17. Dreybrodt, W., Eisenlohr, L., Madry, B. & Ringer, S. Precipitation kinetics of calcite in the system $CaCO_3$-H_2O-CO_2: The conversion to CO_2 by the slow process $H^+ + HCO_3^- \rightarrow CO_2 + H_2O$ as a rate limiting step. *Geochim. Cosmochim. Acta* **61**, 3897-3904 (1997).
18. Liu, Z. & Dreybrod, W. Dissolution kinetics of calcium carbonate minerals in H_2O-CO_2 solutions in turbulent flow: The role of the diffusion boundary layer and the slow reaction $H_2O + CO_2 \rightarrow H^+ + HCO_3^-$. *Geochim. Cosmochim. Acta* **61**, 2879-2889 (1997).
19. Tommaso, D. D. & De Leeuw, N. H. The onset of calcium carbonate nucleation: a density functional theory molecular dynamics and hybrid microsolvation/continuum study. *J. Phys. Chem. B* **112**, 6965-6975 (2008).
20. Gebauer, D. *et al.* Proto-calcite and proto-vaterite in amorphous calcium carbonates. *Angew. Chem. Int. Ed.* **49**, 8889-8891 (2010).
21. Jiang, S. & ter Horst, J. H. Crystal nucleation rates from probability distributions of induction times. *Cryst. Growth & Des.* **11**, 256-261 (2011).
22. Walter, E. D. *et al.* Operando MAS NMR reaction studies at high temperatures and pressures. *J. Phys. Chem. C* **122**, 8209-8215 (2018).
23. Henzler, K. *et al.* Supersaturated calcium carbonate solutions are classical. *Sci. Adv.* **4**, eaao6283 (2018).

24. Raiteri, P., Schuitemaker, A. & Gale, J. D. Ion pairing and multiple ion binding in calcium carbonate solutions based on a polarizable AMOEBA force field and ab initio molecular dynamics. *J. Phys. Chem. B* **124**, 3568-3582, (2020).
25. Baer, M. D. & Mundy, C. J. Local aqueous solvation structure around Ca^{2+} during $Ca^{2+}\cdots Cl–$pair formation. *J. Phys. Chem. B* **120**, 1885-1893 (2016).
26. Fetisov, E. O. *et al.* The statistical mechanics of solution-phase nucleation: $CaCO_3$ revisited. *Found. Mol. Model. Simul*. **2018**, 101-122 (2021).
27. Von Euw, S. *et al.* Biological control of aragonite formation in stony corals. *Science* **356**, 933-938 (2017).
28. Daily, M. D., Baer, M. D. & Mundy, C. J. Divalent ion parameterization strongly affects conformation and interactions of an anionic biomimetic polymer. *J. Phys. Chem. B* **120**, 2198-2208 (2016).
29. Cantaert, B. *et al.* Think Positive: Phase separation enables a positively charged additive to induce dramatic changes in calcium carbonate morphology. *Adv. Funct. Mater.* **22**, 907-915 (2012).
30. Bahn, S. Y., Jo, B. H., Choi, Y. S. & Cha, H. J. Control of nacre biomineralization by Pif80 in pearl oyster. *Sci. Adv.* **3**, e1700765 (2017).
31. Gong, Y. U. *et al.* Phase transitions in biogenic amorphous calcium carbonate. *Proc. Nat. Acad. Sci.* **109**, 6088-6093 (2012).
32. Yao, S. *Et al.* Osteoporotic bone recovery by a highly bone-inductive calcium phosphate polymer-induced liquid-precursor. *Adv. Sci.* **6**, 1900683 (2019).
33. Jee, S.-S., Thula, T. T. & Gower, L. B. Development of bone-like composites via the polymer-induced liquid-precursor (PILP) process. Part 1: influence of polymer molecular weight. *Acta Biomater.* **6**, 3676-3686 (2010).
34. Jin, B. *et al.* Phase transformation mechanism of amorphous calcium phosphate to hydroxyapatite investigated by liquid-cell transmission electron microscopy. *Cryst. Growth & Des.* **21**, 5126-5134 (2021).
35. Rodriguez, D. E. *et al.* Multifunctional role of osteopontin in directing intrafibrillar mineralization of collagen and activation of osteoclasts. *Acta Biomater.* **10**, 494-507 (2014).
36. Olszta, M. J. *et al.* Bone structure and formation: a new perspective. *Mater. Sci. Eng. R: Rep.* **58**, 77-116 (2007).
37. Nudelman, F. *et al.* The role of collagen in bone apatite formation in the presence of hydroxyapatite nucleation inhibitors. *Nat. Mater.* **9**, 1004-1009 (2010).
38. Gower, L. & Tirrell, D. Calcium carbonate films and helices grown in solutions of poly (aspartate). *J. Cryst. Growth* **191**, 153-160 (1998).
39. Gower, L. B. & Odom, D. Deposition of calcium carbonate films by a polymer-induced liquid-precursor (PILP) process. *J. Cryst. Growth* **210**, 719-734 (2000).